Geoscience Frontiers 11 (2020) 2221–2242

HOSTED BY

ELSEVIER

Contents lists available at ScienceDirect

Geoscience Frontiers

journal homepage: www.elsevier.com/locate/gsf

Research Paper

High-pressure metamorphic rocks in the Borborema Province, Northeast Brazil: Reworking of Archean oceanic crust during proterozoic orogenies

Alanielson da Câmara Dantas Ferreira [a,*], Elton Luiz Dantas [a], Ticiano José Saraiva dos Santos [b], Reinhardt A. Fuck [a], Mahyra Tedeschi [c]

[a] *Instituto de Geociências, Universidade de Brasília (UnB), 70910-900, Brasília-DF, Brazil*
[b] *Instituto de Geociências, Universidade Estadual de Campinas (UNICAMP), Departamento de Geologia e Recursos Naturais, 13083-970, Campinas-SP, Brazil*
[c] *Instituto de Geociências, Universidade Federal de Minas Gerais (UFMG), 31270-901, Belo Horizonte, MG, Brazil*

ARTICLE INFO

Handling Editor: Richard M Palin

Keywords:
Archean oceanic crust
Proterozoic orogens
Borborema province

ABSTRACT

We present the first evidence of Archean oceanic crust submitted to Proterozoic high-pressure (HP) metamorphism in the South American Platform. Sm–Nd and Lu–Hf isotopic data combined with U–Pb geochronological data from the Campo Grande area, Rio Grande do Norte domain, in the Northern Borborema Province, reflect a complex Archean (2.9 Ga and 2.6 Ga) and Paleoproterozoic (2.0 Ga) evolution, culminating in the Neoproterozoic Brasiliano/Pan-African orogeny (ca. 600 Ma). The preserved mafic rocks contain massive poikiloblastic garnet and granoblastic amphibole with variable proportions of plagioclase + diopside in symplectitic texture, typical of high-pressure rocks. These clinopyroxene-garnet amphibolites and the more common garnet amphibolites from the Campo Grande area are exposed as rare lenses within an Archean migmatite complex. The amphibolite lenses represent 2.65 Ga juvenile tholeiitic magmatism derived from depleted mantle sources (positive $\varepsilon_{Hf}(t)$ values of +3.81 to +30.66) later enriched by mantle metasomatism (negative $\varepsilon_{Nd}(t)$ values of –7.97). Chondrite and Primitive Mantle-normalized REE of analyzed samples and discriminant diagrams define two different oceanic affinities, with E-MORB and OIB signature. Negative Eu anomalies (Eu/Eu* = 0.75–0.95) indicate depletion of plagioclase in the source. Inherited zircon cores of 3.0–2.9 Ga in analyzed samples indicate that the Neoarchean tholeiitic magmatism was emplaced into 2923 ± 14 Ma old Mesoarchean crust ($\varepsilon_{Nd}(t)$ = –2.58 and Nd T_{DM} = 3.2 Ga) of the Rio Grande do Norte domain. The age of retro-eclogite facies metamorphism is not yet completely understood. We suggest that two high-grade metamorphic events are recognized in the mafic rocks: the first at 2.0 Ga, recorded in some samples, and the second, at ca. 600 Ma, stronger and more pervasive and recorded in several of the mafic rock samples. The Neoproterozoic zircon grains are found in symplectite texture as inclusions in the garnet grains and represent the age of HP conditions in the area. These zircon grains show a younger cluster of concordant analyses between 623 ± 3 Ma and 592 ± 5 Ma with $\varepsilon_{Hf}(t)$ values of +0.74 to –65.88. Thus, the Campo Grande rock assemblage is composed of Archean units that were amalgamated to West Gondwana during Neoproterozoic Brasiliano orogeny continent-continent collision and crustal reworking.

1. Introduction

Precambrian ultrahigh-pressure (UHP) and high-pressure (HP) rocks can be evidence of subduction of ancient oceanic crust similar to modern processes of eclogite formation (e.g. Rubatto and Hermann, 2001; Gordon et al., 2013; Zhang et al., 2019 and references therein). These relicts of oceanic subduction may mark suture zones, allow the identification of distinct magmatic and metamorphic events and suggest geodynamic scenarios for the crustal accretion (e.g. Brown, 2009; McClelland and Lapen, 2013). However, UHP and HP rocks are rare in Precambrian orogens, since tectonic processes tend to subduct mafic residues into the mantle (e.g. Weller and St-Onge, 2017; Zhang et al., 2019). Thus, only a few remain preserved, and these are commonly retrogressed to lower grade metamorphic conditions (e.g. Santos et al., 2009, 2015; Gilotti, 2013; Lanari et al., 2013). An additional reason for the uncommon occurrence of eclogites in Precambrian terranes (e.g. Mints et al., 2010; Li

* Corresponding author.
E-mail address: ferreira.acd@ufrgs.br (A.C.D. Ferreira).
Peer-review under responsibility of China University of Geosciences (Beijing).

https://doi.org/10.1016/j.gsf.2020.03.004
Received 12 April 2019; Received in revised form 7 December 2019; Accepted 9 March 2020
Available online 23 March 2020

et al., 2015; Liu et al., 2017) is that during Archean and Paleoproterozoic times, the geothermal gradient was higher, favoring the occurrence of granulite-facies ultrahigh-temperature metamorphism (G-UHTM) (e.g. Brown, 2009). The opposite scenario occurs in the Phanerozoic orogenic systems, where the medium-temperature eclogite-high-pressure granulite metamorphism is mainly observed (E-HPGM) (e.g. Brown, 2014; Sizova et al., 2014). In addition, the absence of high-pressure and low-temperature metamorphism in the Archean record can also be attributed to the secular changes in oceanic crust composition, i.e., positive correlation between high geothermal gradients and MgO content throughout Earth history (e.g. Palin and White, 2016).

Almost all early mafic crusts were melted (and remelted) to form tonalite-trondhjemite-granodiorite (TTG) associations, which represent nearly 80% of the Archean continental crust (e.g. Rudnick and Gao, 2003; Rollinson, 2010; Moyen and Martin, 2012; Holder et al., 2019). Trace elements contents and neodymium and hafnium isotope data from the scarce Neoarchean tholeiitic basalts with high Nb/Th, Nb/U, Sm/Nd and Lu/Hf ratios suggest mantle depletion in incompatible elements at 2.5 Ga (e.g. Hawkesworth et al., 2010). Independent of plate tectonic and non-plate tectonic models, melting of basaltic crust under amphibolite or eclogite facies is required for the origin of the Archean TTGs (Polat et al., 2011; Polat, 2012). Therefore, the study of tholeiitic basalts (today amphibolites) allows the discussion of important questions like magma source and tectonic setting of the Archean oceanic crust.

Oceanic crust submitted to high-pressure metamorphic conditions (>15 GPa) (e.g. Carswell, 1990) generates eclogites that consist of Na-rich clinopyroxene (omphacite) and commonly Na-rich amphibole. The presence of plagioclase, usually developing symplectitic texture with diopside, indicates the destabilization of omphacite during decompression (e.g. Carswell, 1990). This retrogression stage generates retro-eclogites (e.g., Powell and Holland, 2008; Lanari and Engi, 2017; Tedeschi et al., 2017). In the South American Platform (Fig. 1A), Neoproterozoic retro-eclogites are reported from fold-thrust belt systems in the southern Brasília orogen (e.g. Reno et al., 2012; Trouw et al., 2013) and from the Ceará Central domain (Santos et al., 2009, 2015), northwest portion of the Borborema Province. In both cases, the retro-eclogite occurrences are related to Brasiliano/Pan-African orogeny collision developed during West Gondwana amalgamation. However, in this study, we present the first evidence of tholeiitic mafic crust remnants included in an Archean nucleus in the Borborema Province, NE Brazil. Our study is based on geological mapping, petrographic description, geochemical analyses, Sm–Nd and Lu–Hf isotopic data, and U–Pb geochronology.

2. Geological setting

The Borborema Province (BP) is formed of discontinuous remnants of Archean crust, Paleoproterozoic migmatite-gneiss complexes and Meso- and Neoproterozoic supracrustal rocks (e.g. Jardim de Sá, 1994; Brito Neves et al., 2000; Van Schmus et al., 2008). These units were amalgamated to West Gondwana during the complex and diachronic orogenic collage that took place in distinct pulses from ca. 800 Ma to 500 Ma (e.g. Arthaud et al., 2008; Van Schmus et al., 2008; Brito Neves and Fuck, 2014; Padilha et al., 2017). The position of these diverse crustal fragments during convergence of West African-São Luis and São Francisco-Congo cratons, and the presence of previous zones of weakness, lead to the development of a continental-scale (>200,000 km^2) network of strike-slip shear zones (Fig. 1A) (e.g. Brito Neves et al., 2000; Arthaud et al., 2008; Gray et al., 2008; Santos et al., 2008; Ganade et al., 2014; Padilha et al., 2017). These several shear zones represent local adjustments within each terrain, as well as divide the high-temperature, medium- to low-pressure metamorphic Paleoproterozoic high-grade migmatite-gneiss terranes. The shear zone system was coeval with anatexis processes and synkinematic magmatism, including crust- and mantle-derived magmas (Corsini et al., 1991; Dantas et al., 2004; Arthaud et al., 2008; Brito Neves, 2011; Archanjo et al., 2013; Oliveira and Medeiros, 2018).

The Rio Grande do Norte domain (RGND) is located in the northeastern portion of the Borborema Province (Fig. 1B), and is limited westwards by the NE-trending rectilinear. Portalegre dextral strike-slip shear zone and by the Patos-Adamaoua EW-trending shear zone at the southern boundary (e.g. Jardim de Sá, 1994; Brito Neves, 2011). In the central portion (Fig. 1C), RGND includes Paleoproterozoic basement banded gneiss underlying the Neoproterozoic Seridó schist belt (e.g. Van Schmus et al., 2008; Hollanda et al., 2015; Ferreira et al., 2019). Systematic U–Pb zircon geochronological studies indicate that Rhyacian (2.25–2.15 Ga) metamorphic high-K calc-alkaline magmatic rocks (e.g. Caicó Complex; Souza et al., 2007; Hollanda et al., 2011) and Siderian (2.3 Ga) supracrustal rocks form the basement of the Neoproterozoic Seridó Group (Dantas et al., 2008).

The Campo Grande Archean nucleus is one of the basement inlier of the RGNT (Figs. 1C and 2). The area consists of a migmatitic gneiss complex with supracrustal lenses and intrusive Neoproterozoic granites (e.g. Galindo, 1993; Trindade et al., 1999). In this area (Fig. 2), we discovered amphibolite lenses with preserved textures that we interpret as evidence of high-pressure mafic rocks inside an Archean basement in South America, a distinct setting from all retro-eclogites previously described within Neoproterozoic supracrustal sequences in West Gondwana.

3. Materials and methods

3.1. Geological mapping and petrography

Geological mapping in the Campo Grande area was carried out from 2016 to 2018 with the purpose of investigating the mafic bodies inserted in the gneiss-migmatite complex. Geological mapping was supported by geochronology, geochemical, geophysical and petrographic surveys. Systematic thin sections cut relative to foliation were obtained from representative samples from fourteen outcrops of mafic lenses and host migmatite and investigated in the Microscopy Laboratory of the Institute of Geosciences of Universidade de Brasília (Brazil). These samples are from mafic lenses with a high modal concentration of pyroxene and garnet, since most mafic rock outcrops consist almost exclusively of amphibole and plagioclase, recording full retrogression of the HP mineral assemblage.

3.2. Geochemistry

Geochemical analyses were performed on 16 samples of the mapped mafic rocks. Analyses of major and trace elements were carried out by ACME Analytical Laboratories (Vancouver, Canada). Major and minor elements were obtained by X-ray fluorescence (XRF) after fusion of the sample with lithium tetraborate. Trace elements were determined from melting 0.2 g of the sample with lithium metaborate/tetraborate, diluted nitric acid digestion and ICP-OES analysis. The loss on ignition (LOI) was given by weight difference after heating at 100 °C. Precious metals and base metals were determined after 0.5 g of sample digestion with Acqua Regia with ICP-MS analysis.

3.3. U–Pb and Lu–Hf isotopes

Zircon grains from mafic lenses and host migmatite-gneiss were separated by density and magnetic separator before concentration by hand picking to assemble the grain mounts. U–Pb and Lu–Hf isotopic analyses were performed on zircon grains using a Thermo-Fisher Neptune High Resolution Multicollector Inductively Coupled Plasma Mass Spectrometer (HR-MC-ICP-MS) coupled with a Nd:YAG UP213 New Wave laser ablation system at the Laboratory of Geochronology of Universidade de Brasília. U–Pb analyses on zircon grains were carried out by the standard-sample bracketing method (Albarède et al., 2004), using the GJ-1 standard zircon (Jackson et al., 2004) in order to quantify the amount of ICP-MS fractionation. The tuned masses were 238, 207, 206,

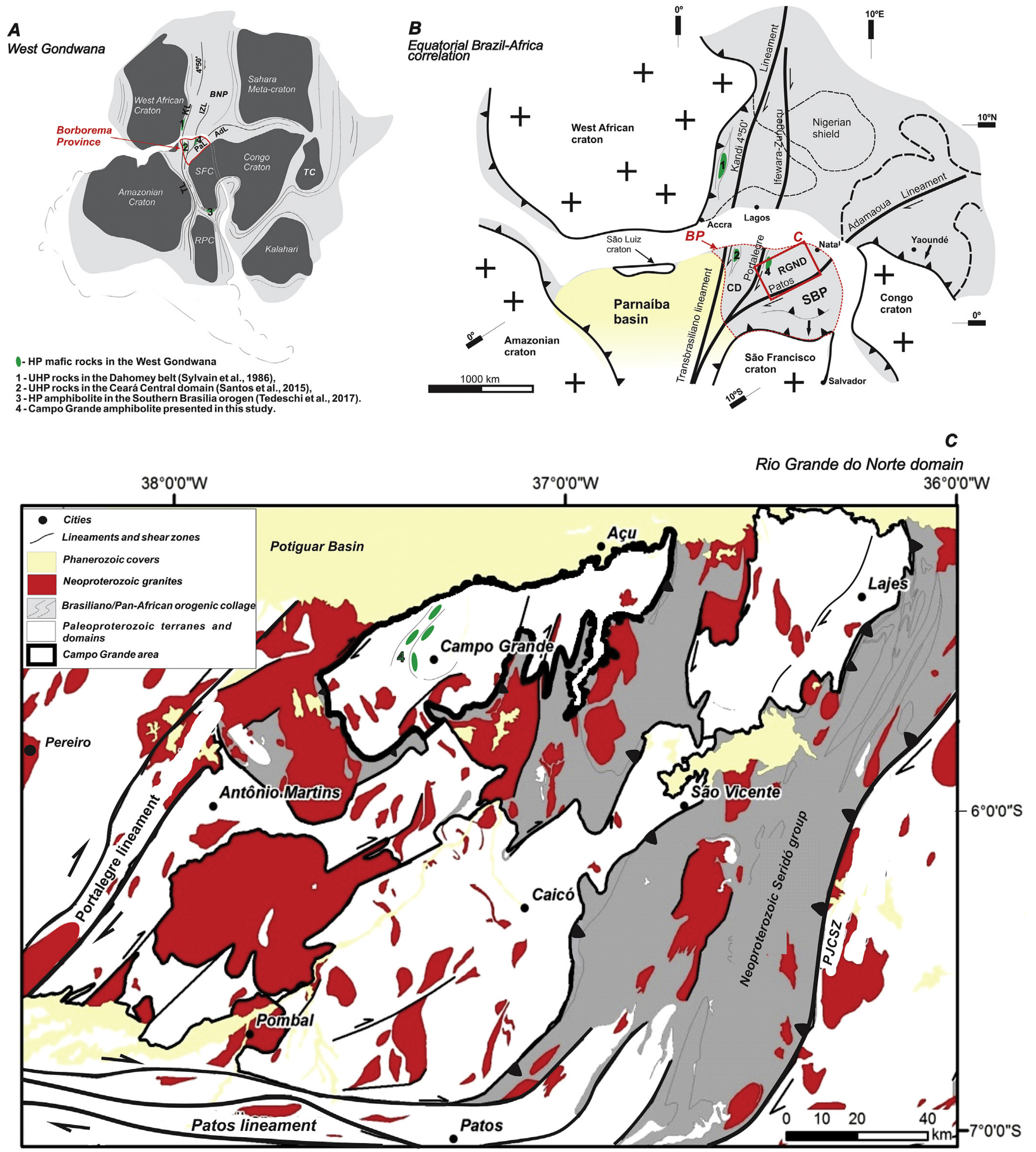

Fig. 1. Regional geological setting. (A) Localization map of the Borborema Province (BP) in West Gondwana. BNP–Benin-Nigeria Province, RPC–Rio de La Plata Craton, SFC–São Francisco Craton, TC–Tanzania Craton, TL–Transbrasiliano Lineament, KL–Kandi Lineament, IZL–Ifewara-Zungeru Lineament, PaL–Patos Lineament, ADL–Adamaoua Lineament (modified from Gray et al., 2008; Brito Neves and Fuck, 2014; Ganade et al., 2016). (B) Equatorial Brazil-Africa correlation modified from Jardim de Sá (1994) and Van Schmus et al. (2008). CD–Ceará domain, RGND–Rio Grande do Norte domain, and SBP–Southern Borborema Province. (C) Geological map of the Rio Grande do Norte domain modified from Jardim de Sá (1994). PJCSZ–Picuí-João Câmara shear zone.

204 and 202. The integration time was 1 s and the ablation time was 40 s. A 30 μm spot size was used and the laser setting was 10 Hz and 2–3 J/cm^2. Two to four unknown grains were analyzed between GJ-1 analyses. $^{206}Pb/^{207}Pb$ and $^{206}Pb/^{238}U$ ratios were time corrected. The raw data were processed off-line and reduced using an Excel worksheet (Bühn et al., 2009). During the analytical sessions, the zircon standard 91500 (Jackson et al., 2004) was also analyzed as an external standard.

Common ^{204}Pb was monitored using the ^{202}Hg and ($^{204}Hg + ^{204}Pb$)

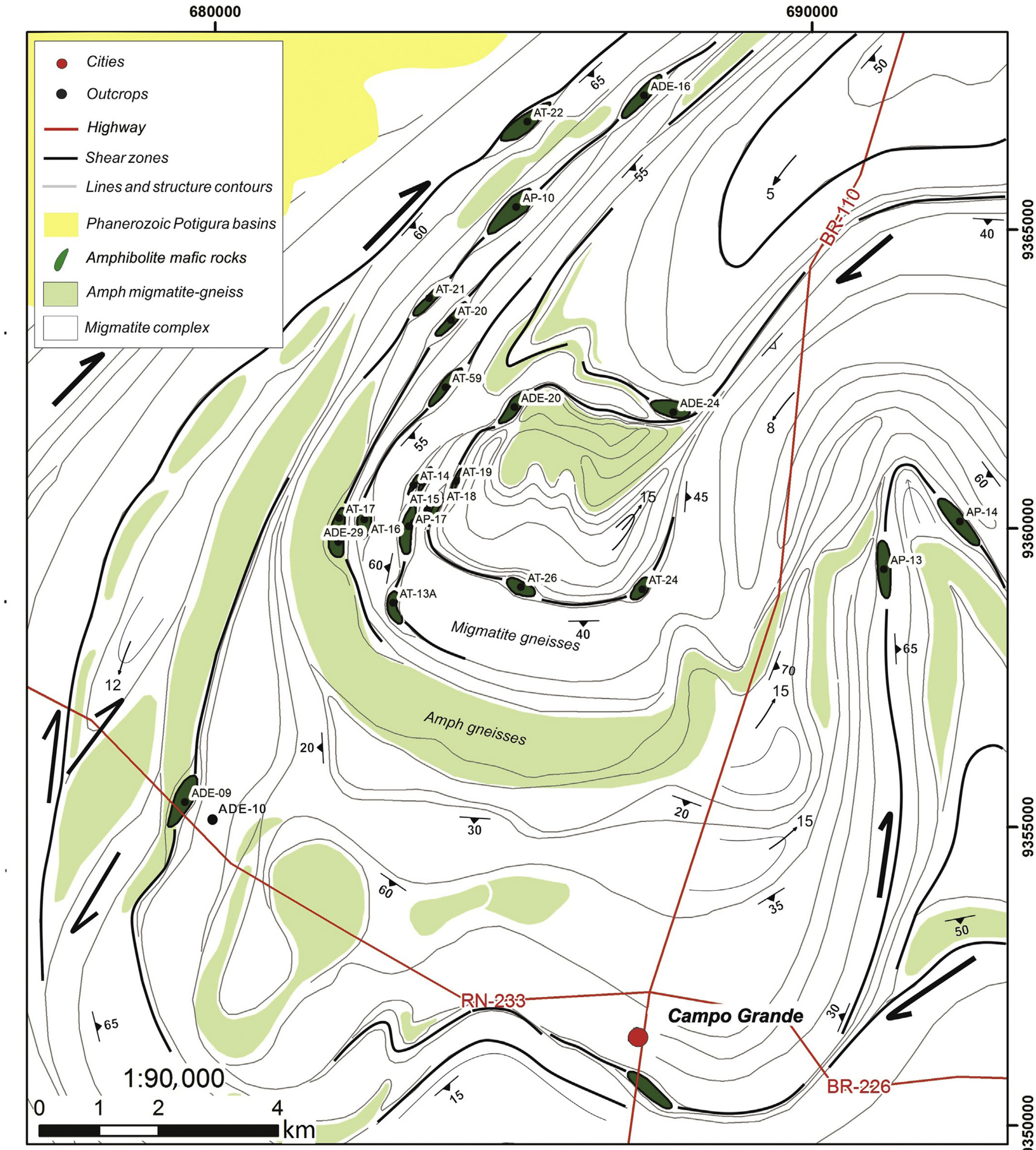

Fig. 2. Simplified geological map of the Campo Grande area. The Campo Grande area represents an ellipsoidal gneissic-migmatitic block generated due to the combined stresses related to eastward push from the Neoproterozoic Portalegre shear zone and northward push from the Neoproterozoic Patos shear zone, which produced NW–SE shortening and amalgamation/accretion of allochthonous terranes, leading to an extensive network of dextral strike-slip shear zones.

masses. Common Pb corrections were not done due to very low signals of ^{204}Pb (<30 cps) and high ^{206}Pb/^{204}Pb ratios. Reported errors are propagated by quadratic addition [$(2SD^2+2SE^2)/2$] (SD = standard deviation; SE = standard error) of external reproducibility and within-run precision. External reproducibility is represented by the standard deviation obtained from repeated analyses (~1.1% for ^{207}Pb/^{206}Pb and up to ~2% for ^{206}Pb/^{238}U) of the GJ-1 zircon standard during the analytical sessions, and the within-run precision is the standard error calculated for each analysis. Concordia diagrams (2σ error ellipses), probability density plots and weighted average ages were calculated using the Isoplot-3/Ex software (Ludwig, 2008).

Zircon crystals previously analyzed for U–Pb isotopes and showing concordant to slightly discordant (<10%) data were selected for Lu–Hf analyses. Lu–Hf isotopic data were collected over 50 s of ablation time and using a 50 μm spot size. During the analytical sessions, replicate analyses of the GJ-1 standard zircon were performed, obtaining an average $^{176}Hf/^{177}Hf$ ratio of 0.282006 ± 16 (2σ), in good agreement with the reference value for the GJ standard zircon (Morel et al., 2008). Measurement spots were carefully positioned in the same growth area but not onto the same spot analyzed for U–Pb data. The signals of the interference-free isotopes ^{171}Yb, ^{173}Yb and ^{175}Lu were monitored during analysis in order to correct for isobaric interferences of ^{176}Yb and ^{176}Lu on the ^{176}Hf signal. The ^{176}Yb and ^{176}Lu contributions were calculated using the isotopic abundance of Lu and Hf (Chu et al., 2002). Contemporaneous measurements of ^{171}Yb and ^{173}Yb provide a method to correct for mass-bias of Yb using a $^{173}Yb/^{171}Yb$ normalization factor of 1.132685 (Chu et al., 2002). The Hf isotope ratios were normalized to $^{179}Hf/^{177}Hf$ of 0.7325 (Patchett, 1983). $\varepsilon_{Hf}(t)$ was calculated using the decay constant $\lambda = 1.865 \times 10^{-11}$(Scherer et al., 2001) and the $^{176}Lu/^{177}Hf$ and $^{176}Hf/^{177}Hf$ CHUR values of 0.0332 and 0.282772 (Blichert-Toft and Albarède, 1997), respectively. Two-stage model ages (T_{DM}) were calculated from the initial Hf isotopic composition of zircon, using an average crustal Lu/Hf ratio (e.g. Gerdes and Zeh, 2009). The values of $^{176}Lu/^{177}Hf = 0.0384$ and $^{176}Hf/^{177}Hf = 0.28325$ were used for depleted mantle (Chauvel and Blichert-Toft, 2001), and $^{176}Lu/^{177}Hf = 0.0113$ for average crust (Wedepohl, 1995).

The Lu–Hf system is analogous to the Sm–Nd isotopic system (e.g. Vervoort and Blichert-Toft, 1999) and provides an unparalleled time series of changing magmatic and metamorphic conditions during crystal growth (e.g. Hawkesworth and Kemp, 2006). The zircon grains preserve the initial $^{176}Hf/^{177}Hf$ isotopic ratios inherited by the magma from which they crystallized. Since zircon is highly robust and has high Hf contents (1%–3%), Hf isotope ratios are largely impervious to deep weathering, deformation and alteration, all of which can disturb bulk rock isotope systems, including Sm–Nd (e.g. Hawkesworth and Kemp, 2006).

The analyzed zircon grains are rounded and unzoned (50–100 μm) to elongated (100–200 μm) with length/width ratio of 2:1 and 3:1, respectively. Images of the selected zircon grains in backscattered electrons (BSE) mode were obtained using a Scanning Electron Microprobe (SEM) in order to gather information on the internal structure of the studied grains. The BSE images allow to differentiate between Hf-rich (bright) and Hf-poor (less bright) portions of the zircon grains. In addition, studied zircon grains from the amphibolite samples show unzoned Hf-poor cores rimmed by Hf-rich rims.

Depleted mantle hafnium model ages give a qualitative estimate of the time of separation of the source rocks (e.g. Hawkesworth and Kemp, 2006). Therefore, depleted mantle model ages do not necessarily provide any real age information. However, Hf T_{DM} with $\varepsilon_{Hf}(t)$ values are useful in identifying older crustal versus juvenile magmatic contributions (e.g. Nebel et al., 2007; Gerdes and Zeh, 2009).

3.4. Sm–Nd isotopes

Sm–Nd isotopic analyses followed the method described by Gioia and Pimentel (2000) and were also carried out at the Geochronology Laboratory of Universidade de Brasília. Whole-rock powders (~50 mg) of 11 representative samples were mixed with $^{149}Sm–^{150}Nd$ spike solution and dissolved in Savillex Digestion Vessels. Sm and Nd extraction of whole-rock samples followed conventional cation exchange chromatography techniques, with Teflon columns containing LN-Spec resin (HDEHP – diethylhexil phosphoric acid supported on PTFE powder). Sm and Nd fractions were loaded on Re evaporation filaments of double filament assemblies, and the isotopic measurements were carried out on a multicollector TRITON thermal ionization mass spectrometer in static mode. Uncertainties of Sm/Nd and $^{143}Nd/^{144}Nd$ ratios were better than ±0.1% (2σ standard error) and ±0.0015% (1σ), respectively, according to repeated analyses of the international rock standard BHVO-1. $^{143}Nd/^{144}Nd$ ratios were normalized to $^{146}Nd/^{144}Nd = 0.7219$, and the decay constant used was 6.54×10^{-12}. The T_{DM} values were calculated using the model of DePaolo (1981).

4. Results

4.1. Field relationships and petrography

Field description was based on mafic rocks found in outcrops in the Campo Grande area, central portion of Rio Grande do Norte State, Northeast Brazil. These rocks comprise clinopyroxene-garnet amphibolites that crop out as discontinuous lenticular bodies, forming boudins, with variable sizes (~30 cm–120 m long) (Fig. 2). The amphibolite boudins are hosted in a migmatite-gneiss complex (Figs. 3A and 4A), which includes alkali biotite to amphibole-biotite migmatite-gneiss, clinopyroxenite and paragneiss. The amphibolite outcrops form a lenticular pattern of concordant mafic bodies parallel to foliation of the host migmatites. They also occur as isolated lenses within the N–NE to E–W trending shear zone systems (Fig. 2) that underline the ellipsoid shape of the Campo Grande Block. Garnet-biotite paragneiss layers, calc-silicate rocks, and alkaline granite intrusions also occur in the study area.

In the core portions, the mafic rocks are medium- to coarse-grained and contain garnet porphyroblasts (15%–25%) with 200–800 μm, and granoblastic amphibole (25%–45%), with variable proportions of plagioclase + clinopyroxene + amphibole (35%–45%), forming a typical symplectitic texture (Fig. 3C–H) within the inner domains of the bodies. The symplectitic texture is a typical indication of a high-pressure metamorphic event (e.g. Santos et al., 2009, 2015; Tedeschi et al., 2017). Garnet with symplectitic overgrowth of plagioclase + clinopyroxene + amphibole represents the retrograded HP mineral assemblage. However, most mafic rock outcrops consist mainly of granoblastic amphibole (ca. 60%) and plagioclase (ca. 40%), recording full retrogression of the former mineral assemblage. These rocks show medium- to fine-grained texture towards their rims, which are foliated due to deformation related to the development of shear zones (Fig. 4A).

Garnet crystals exhibit irregular shapes with lobate edges, and a composite corona texture is developed on their borders, composed of an inner plagioclase and an outer amphibole corona. The garnet porphyroblasts display inclusions of quartz, ilmenite, clinopyroxene and zircon (Fig. 3C). Garnet grains are irregular in shape due to breakdown reaction rims imposed by retrogression. The deformation is better observed in outcrop-scale mainly by the boudinage process along the Campo Grande shear zones systems, indicating that the emplacement of these mafic rocks was coeval or prior to the last deformation. Thus, zircon inclusions in garnet may represent the time of the HP metamorphism or the previous phases recorded in the protolith sources or the host migmatite.

Clinopyroxene occurs as subhedral crystals in contact with amphibole or developing symplectitic texture with plagioclase and amphibole. Amphibole occurs by replacing both primary and secondary pyroxene and garnet crystals as vermicular fine-grained crystals in symplectite, inclusions in granoblastic garnet and developed corona texture (Fig. 3C–H). Plagioclase grains occur in the symplectite and corona texture. Rutile, ilmenite, apatite, zircon and titanite are accessory minerals (<3%). Quartz inclusions were examined by Raman spectroscopy, but high-pressure polymorphs (e.g. coesite) were not found. Some lenses are completely retrograded, marked by the increase in amphibole concentration. The amphibolite rims show the same tectonic foliation imprinted in the host gneiss complex. Sometimes, 3–5 m wide shear zones characterize the contact between mafic rocks and gneisses (Fig. 4A).

The country rocks comprise mainly deformed tonalitic paleosome (Fig. 4B) and garnet-biotite gneiss (Fig. 4C). Melanosome bands consist of biotite (40%–50%) and amphibole (5%–15%), with feldspar (5%–10%) and quartz (15%–25%) porphyroclasts surrounded by biotite and red garnet (3%–5%) porphyroblasts. The leucosome bands are composed of microcline (20%–30%) and plagioclase (30%–40%) with quartz ribbons (30%–40%), forming augen textures and making up the major part of the

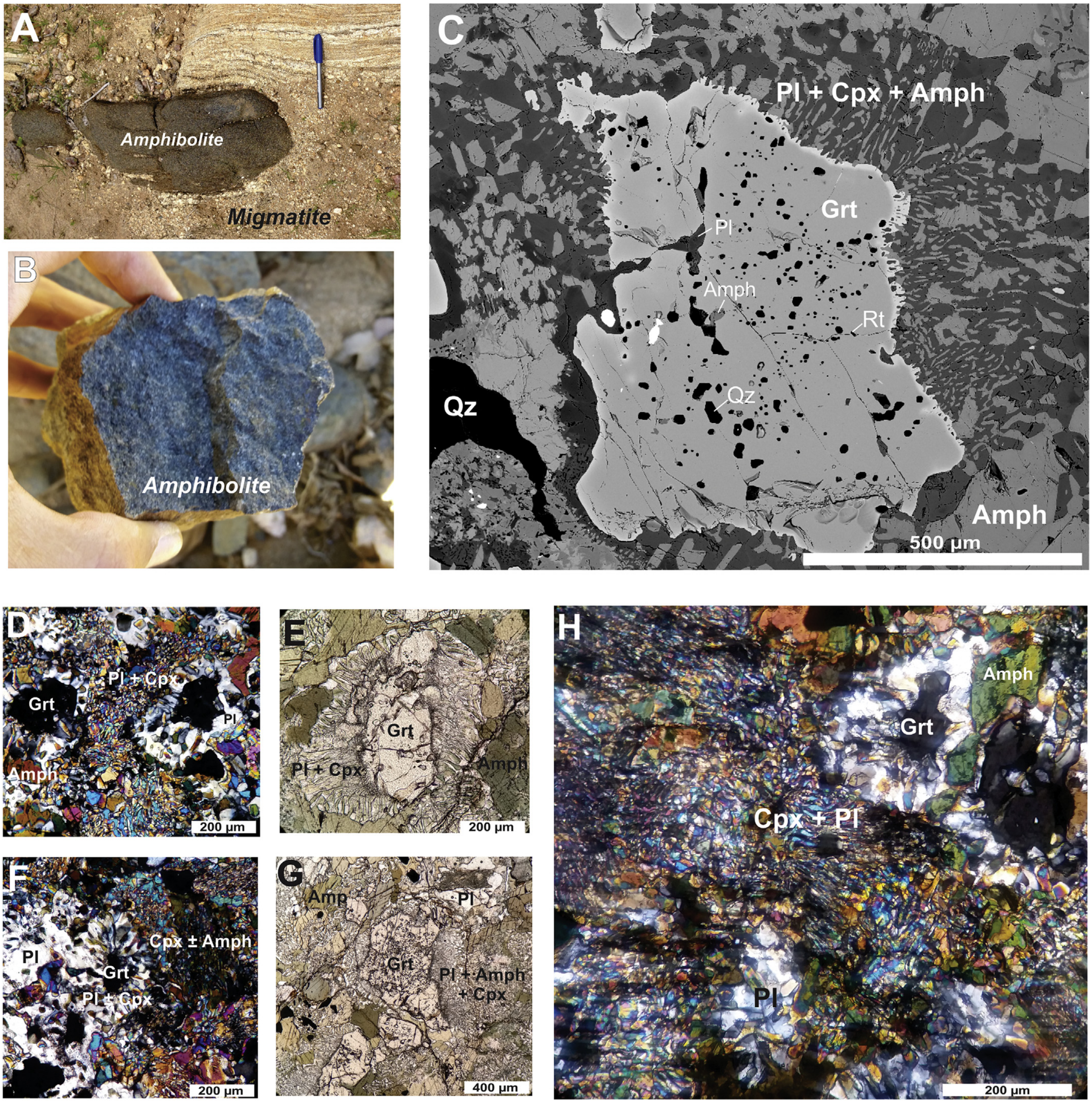

Fig. 3. Petrographic features and symplectitic texture of the Campo Grande amphibolites. (A) AP-10 mafic lens parallel to foliation of the host migmatite. (B) Hand ADE-20 sample. (C) Symplectitic texture in scanning electron microscope image of sample AP-14. Photomicrographs of (D) Sample ADE-16, (E) Sample ADE-24B, (F) Sample ADE-20, (G) Sample AP-17, (H) Petrographic features and symplectitic texture of the ADE-29 sample. (D, E, F, H) Crossed polarizers, (G) parallel polarizers. Mineral symbols follow Whitney and Evans (2010).

felsic layers. Ilmenite, apatite and zircon are accessory mineral phases in the leucosome. Garnet crystals from gneiss exhibit a pseudo-automorphic shape (Fig. 4D) with some lobed edges and quartz inclusions, while pressure shadows host biotite growths. Sometimes the idiomorphic shape of the garnet crystals indicates deformation and resorption (Fig. 4E), with feldspar and biotite along the mylonitic zone.

4.2. Geochemistry

Sixteen amphibolite samples were selected for geochemical analyses in the study area (see localization in Fig. 2 and Supplementary Table 1). The samples were collected mainly in the central portions of the mafic boudins, where features indicating retrogression of HP mineral assemblages are preserved. Whole-rock chemical compositions of representative samples of the investigated amphibolites are listed in Table 1. The plot of major element oxides (Al_2O_3, Na_2O, CaO, Fe_2O_3, P_2O_5, TiO_2 and K_2O) against the Mg# (= Mg/(Mg+Fe) × 100) (Fig. 5A–G) indicates that bulk compositions are mainly controlled by different amounts of amphibole, garnet, clinopyroxene and plagioclase in the mafic rock. Thus, samples rich in Na_2O and CaO have higher modal concentrations of

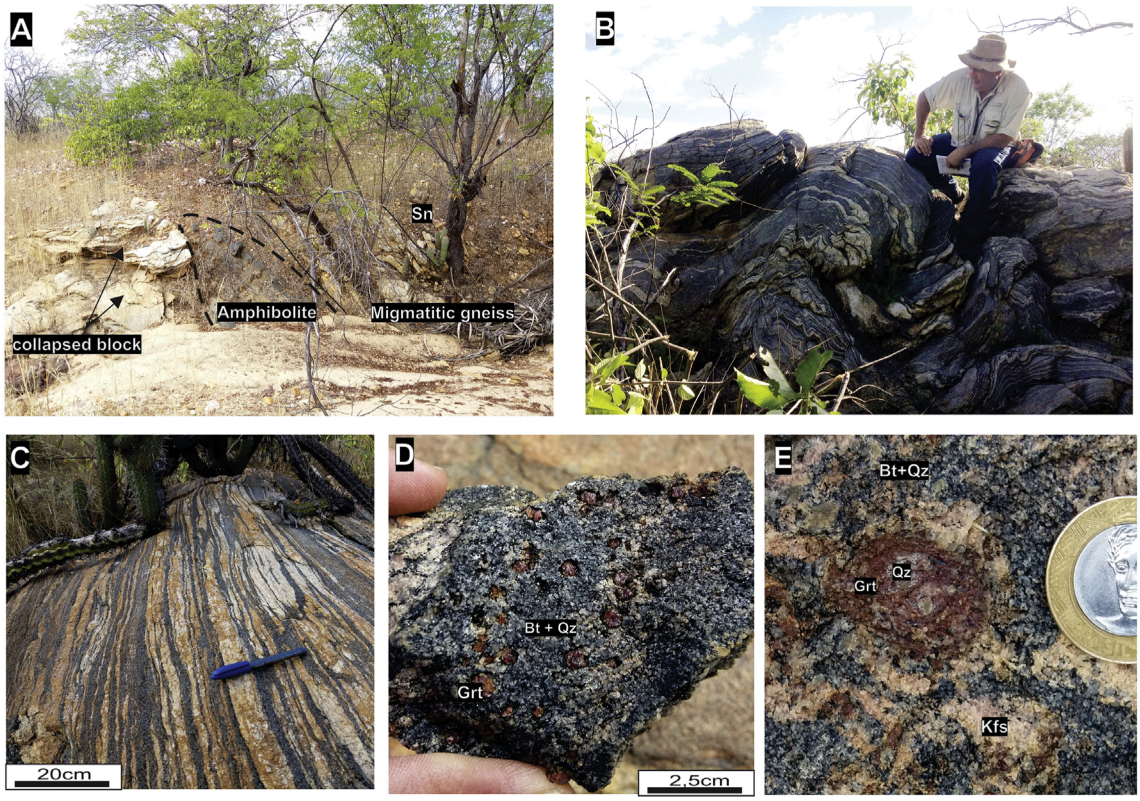

Fig. 4. Field views of amphibolites and host gneiss. (A) AT-26 mafic lens concordant and parallel to low-angle Sn foliation dipping 35° to the south. (B) Strongly folded stromatic structure of tonalitic paleosome (sample ADE-10). (C) Strongly deformed garnet-biotite gneiss along a NE–SW-trending shear zone. (D) Hand sample of garnet-biotite gneiss showing garnet crystals with pseudo-automorphic shape and some lobed edges. (E) Syntectonic garnet porphyroblast with internal zonation (helicitic inclusion trails) that indicate top-to-the-SW rotation of more than 180°. Mineral symbols follow Whitney and Evans (2010).

clinopyroxene, while samples with high FeO have higher Fe-amphibole content. In addition, lower K_2O content corroborates the absence of K-bearing minerals. Mg# was used as an index of fractionation because it largely reflects the changes in the samples MgO content (e.g. Hills and Haggerty, 1989; Defant and Drummond, 1990; Jacob, 2004).

Bivariate diagrams were used to characterize the sources and investigate the protolith evolution. These diagrams (Fig. 5A–G) indicate that amphibolite protoliths crystallized from fractionated mafic magmas with Mg# between 40.9 and 54.56, high Al_2O_3 (13.4–15.4 wt.%) and CaO (9.77–11.90 wt.%) and low Fe_2O_3 (10.65–15.19 wt.%). A more fractionated sample group was observed, with lower Al_2O_3 (<13.95 wt.%), CaO (<5.67 wt.%) and Mg# ranging between 30.06 and 37.15, with higher Fe_2O_3 (14.55–20.70 wt.%), P_2O_5 (0.19–0.45 wt.%) and TiO_2 (1.78–3.21 wt.%). The group with lower Mg# has high Th (1.38–8.11 ppm), Ba (65.7–599 ppm) and Rb (4–47.6 ppm) when compared to the group with higher Mg# that shows low Th (0.3–3.24 ppm), Ba (20–310 ppm) and Rb (0.9–13.5 ppm). The high Mg# group has a higher concentration (60%–80%) of garnet and pyroxene with well-developed symplectitic texture, whereas the lower Mg# group consists mainly of granoblastic amphibole. The samples in both groups, more fractionated and more primitive, have relatively low contents of K_2O (~0.1 wt.%) and low concentration of lithophile elements (Table 1). These samples also have tholeiitic affinity (Fig. 6A) (Irvine and Baragar, 1971) and sub-alkaline basaltic composition, with low $Na_2O + K_2O$ (0.99–4.38 wt.%), Si_2O (46.9–56.1 wt.%), Zr/Ti (0.007–0.02) and Nb/Y (0.1–0.8) ratios (Fig. 6B) (Pearce, 2008).

Chondrite-normalized rare earth elements (REE) profiles show a similar pattern to fractionated E-MORB from Sun and McDonough (1989) for the higher Mg# samples (Fig. 7A). These REE profiles have distinctively positive slopes for light REE, $(La/Yb)_N = 1.62–3.10$, and flat distribution of heavy REE, $(Tb/Yb)_N = 0.91–1.27$. The lower Mg# group shows a similar pattern to ocean island basalts (OIB) (Fig. 7A) with higher enrichment of LREE, $(La/Yb)_N = 1.92–8.34$, and HREE, $(Tb/Yb)_N = 1.17–1.89$. A negative Eu anomaly ($Eu/Eu^* = 0.75–1.06$) indicates plagioclase depletion in both amphibolite groups sources.

Primitive mantle normalized trace elements profiles exhibit slight enrichment of Cs, Ba, Th, U, La, Pb and LREE (as Dy, Yb and Lu), and depletion of Rb, Nb, K, Sr, and Ti in relation to the E-MORB pattern (Fig. 7B). The samples are enriched in Dy, Y, Yb and Lu in comparison to the OIB pattern, while the other elements are depleted (Fig. 7B). Pb shows the strongest fractionation in relation to the E-MORB and OIB patterns.

In the TiO_2–K_2O–P_2O_5 diagram (Pearce et al., 1975), amphibolite samples plot in the oceanic basalt field (Fig. 8A), with the exception of samples AT-02 and AP-14A, which high Ba (117 ppm and 564 ppm) and Sr (152 ppm and 551 ppm). The Hf/3–Nb/16–Th ternary discrimination diagram (Wood, 1980) shows that most samples plot in the D field of island arc tholeiite; progressive enrichment of Th shifts samples from E-MORB to arc-basalts (Fig. 8B). In the Nb×2–Zr/4–Y diagram (Meschede, 1986), amphibolite samples also plot in the N-MORB to volcanic arc basalts fields (Fig. 8C). Thus, discriminant diagrams corroborate an oceanic crust, with E-MORB and OIB signatures, as source of the studied mafic rocks.

4.3. U–Pb geochronology

Six amphibolite samples and one host tonalitic paleosome gneiss sample were dated (Supplementary Table 2). The samples were selected based on the presence of porphyroblastic garnet surrounded by symplectitic growth of plagioclase + clinopyroxene + amphibole that may represent the retrograded HP mineral assemblage, and the spatial distribution of the samples to map the geochronological extension of the

Table 1
Whole-rock analyses of representative samples from the Campo Grande amphibolite (major elements in wt.% and trace elements in ppm).

Sample	ADE-09	ADE-29	AT-20	AT-10	AT-16	ADE-16	AP-10	AT-26	ADE-24A	AT-24	ADE-24B	ADE-20	AT-02	AP-14B	AP-14A	AP-17
SiO_2	48.80	49.20	46.90	56.10	47.90	50.83	48.20	50.60	52.05	55.60	50.70	54.00	53.60	48.90	49.80	51.10
Al_2O_3	14.00	15.07	11.80	13.95	14.90	13.70	13.40	14.95	15.07	15.05	14.10	14.65	15.40	14.75	13.05	13.00
Fe_2O_3	13.50	14.10	20.70	15.95	17.10	15.19	16.30	14.00	11.49	10.45	12.45	12.55	10.65	12.50	14.55	18.25
MnO	0.20	0.21	0.25	0.25	0.24	0.22	0.21	0.20	0.18	0.16	0.22	0.22	0.21	0.20	0.20	0.25
MgO	7.11	6.59	4.99	4.67	5.67	5.92	7.06	6.42	5.69	5.37	6.43	6.54	5.68	8.42	4.36	4.70
CaO	10.65	10.36	9.37	7.17	9.46	10.01	11.00	10.15	11.02	11.05	11.90	11.25	9.77	11.20	7.40	8.71
Na_2O	2.25	2.57	1.24	0.90	2.58	2.14	1.88	2.86	2.42	1.62	2.54	1.19	3.61	0.96	2.83	1.47
K_2O	0.17	0.19	0.39	0.09	0.39	0.13	0.07	0.55	0.17	0.11	0.18	0.09	0.76	0.19	1.71	0.41
P_2O_5	0.14	0.14	0.25	0.21	0.19	0.20	0.23	0.13	0.15	0.08	0.16	0.06	0.06	0.11	0.45	0.34
TiO_2	1.26	1.30	3.01	1.47	1.78	1.62	1.76	1.37	1.08	0.64	1.12	0.71	0.71	0.88	3.21	2.92
Cr_2O_3	0.04	0.05	<0.01	0.01	0.01	0.03	0.04	0.03	0.01	0.04	0.02	0.03	0.06	0.05	0.01	0.01
LOI	0.45	0.00	0.26	0.12	0.30	0.20	0.11	0.57	0.40	0.14	0.61	−0.02	1.01	1.00	2.41	0.20
TOTAL	98.60	99.79	98.65	100.96	100.54	99.80	100.28	101.87	99.75	100.33	100.46	101.28	101.53	99.17	100.11	101.41
Mg#	48.42	45.45	30.06	34.29	37.15	40.99	43.57	44.98	46.89	47.81	47.93	48.16	48.74	54.56	34.82	31.46
Sc	39.00	35.00	45.00	38.00	37.00	37.00	40.00	36.00	33.00	38.00	36.00	44.00	31.00	35.00	27.00	37.00
V	269.00	268.00	726.00	341.00	353.00	270.00	346.00	294.00	251.00	229.00	302.00	316.00	235.00	262.00	449.00	449.00
Cr	280.00	<10	<10	60.00	80.00	<10	300.00	170.00	<10	240.00	130.00	220.00	420.00	360.00	70.00	80.00
Co	83.00	56.80	113.00	116.00	91.00	55.90	60.00	70.00	66.50	88.00	70.00	81.00	46.00	76.00	41.00	68.00
Ni	102.00	89.00	71.00	65.00	94.00	64.00	117.00	104.00	124.00	47.00	120.00	65.00	176.00	105.00	43.00	62.00
Cu	28.00	94.90	329.00	128.00	155.00	102.60	61.00	85.00	61.20	107.00	45.00	149.00	85.00	10.00	127.00	461.00
Zn	101.00	7.00	124.00	78.00	120.00	6.00	181.00	107.00	5.00	61.00	96.00	76.00	105.00	92.00	134.00	147.00
Ga	17.30	16.70	21.70	16.60	22.40	15.60	16.80	19.00	17.40	16.10	17.50	14.80	20.60	17.10	24.90	22.60
Rb	1.80	4.20	12.40	4.00	11.90	2.20	0.90	13.50	2.60	2.60	2.60	2.00	8.70	5.30	47.60	23.80
Sr	79.40	95.10	64.80	64.50	121.00	71.40	68.40	127.50	492.80	221.00	99.70	78.50	152.50	37.20	551.00	132.50
Y	29.80	28.00	42.10	42.80	35.00	33.30	45.70	25.60	33.80	31.50	38.00	26.20	28.00	25.10	38.40	59.40
Zr	118.00	90.50	126.00	151.00	115.00	162.10	156.00	75.00	115.60	66.00	129.00	81.00	32.00	66.00	289.00	314.00
Nb	6.00	4.40	8.70	10.30	10.40	8.80	12.30	6.80	6.80	4.40	6.60	4.90	9.80	5.30	22.70	20.30
Cs	0.18	0.20	0.63	0.24	0.37	0.10	0.08	1.08	<0.1	0.11	0.17	0.17	0.34	0.44	0.79	2.16
Ba	199.50	35.00	65.70	599.00	181.00	20.00	118.00	310.00	179.00	109.50	93.90	29.10	117.00	109.00	564.00	324.00
Hf	3.10	2.60	3.40	3.90	3.20	4.20	4.20	2.00	3.30	1.90	3.30	2.30	1.30	1.70	7.20	8.20
Ta	0.80	0.30	0.80	1.00	0.80	0.60	0.80	0.50	0.60	0.50	0.70	0.90	1.10	0.40	1.40	1.40
Pb	<	0.10	<	<	<	0.50	4.00	23.00	5.30	18.00	2.00	4.00	11.00	3.00	6.00	6.00
Th	0.30	0.70	1.38	8.11	1.73	2.60	1.79	0.66	2.40	3.24	1.90	2.56	1.60	0.72	4.30	4.45
U	0.34	0.20	0.58	1.71	0.29	0.70	0.42	0.19	0.90	0.74	0.81	0.45	1.66	0.21	0.90	1.11
La	7.30	7.80	11.40	22.30	16.20	14.00	14.30	10.40	11.90	18.80	10.90	8.40	19.30	7.20	34.90	31.60
Ce	17.70	18.00	26.60	47.50	31.70	31.30	32.50	16.90	31.60	32.60	23.80	17.60	53.70	13.90	76.20	61.30
Pr	2.46	2.46	3.41	5.51	4.30	3.78	4.56	2.40	3.51	4.07	3.50	2.26	4.33	1.94	10.65	8.87
Nd	11.20	12.10	16.10	22.70	19.80	15.80	20.60	11.70	15.40	16.80	15.70	9.10	17.20	8.90	43.70	38.80
Sm	3.10	3.16	4.44	5.70	5.04	4.00	5.19	2.97	3.93	4.23	4.35	2.32	3.85	2.63	9.44	9.21
Eu	1.12	1.27	1.57	1.53	1.89	1.36	1.65	1.30	1.38	1.65	1.34	0.66	1.02	1.23	2.83	2.67
Gd	4.52	4.25	6.36	6.64	6.08	5.00	7.12	4.19	4.93	5.45	6.13	3.10	4.33	3.64	8.74	10.75
Tb	0.78	0.76	1.10	1.14	1.01	0.89	1.17	0.67	0.89	0.90	1.04	0.59	0.76	0.65	1.25	1.55
Dy	4.89	5.10	6.95	7.21	6.11	6.07	7.56	4.35	5.89	5.20	6.28	3.89	4.87	4.11	7.00	9.79
Ho	1.12	1.05	1.49	1.53	1.28	1.28	1.65	0.89	1.26	1.06	1.40	0.94	1.03	0.87	1.41	2.16
Er	3.38	3.09	4.40	4.37	3.67	3.69	4.93	2.56	3.61	3.23	4.37	3.16	2.84	2.54	3.80	6.34
Tm	0.44	0.44	0.64	0.65	0.56	0.56	0.72	0.37	0.56	0.49	0.63	0.50	0.45	0.36	0.52	0.89
Yb	3.23	2.88	4.26	3.97	3.48	3.58	4.65	2.41	3.59	3.02	3.80	2.95	2.84	2.33	3.00	5.65
Lu	0.44	0.47	0.66	0.61	0.51	0.53	0.69	0.35	0.56	0.51	0.56	0.44	0.43	0.33	0.46	0.82
$(La/Yb)_N$	1.62	1.94	1.92	4.03	3.34	2.81	2.21	3.10	2.38	4.47	2.06	2.04	4.87	2.22	8.34	4.01
$(La/Sm)_N$	1.52	1.59	1.66	2.53	2.08	2.26	1.78	2.26	1.95	2.87	1.62	2.34	3.24	1.77	2.39	2.21
$(Tb/Yb)_N$	1.10	1.20	1.17	1.31	1.32	1.13	1.14	1.26	1.13	1.35	1.24	0.91	1.22	1.27	1.89	1.25
Eu/Eu*	0.91	1.06	0.90	0.76	1.04	0.93	0.83	1.13	0.96	1.05	0.79	0.75	0.76	1.21	0.95	0.82

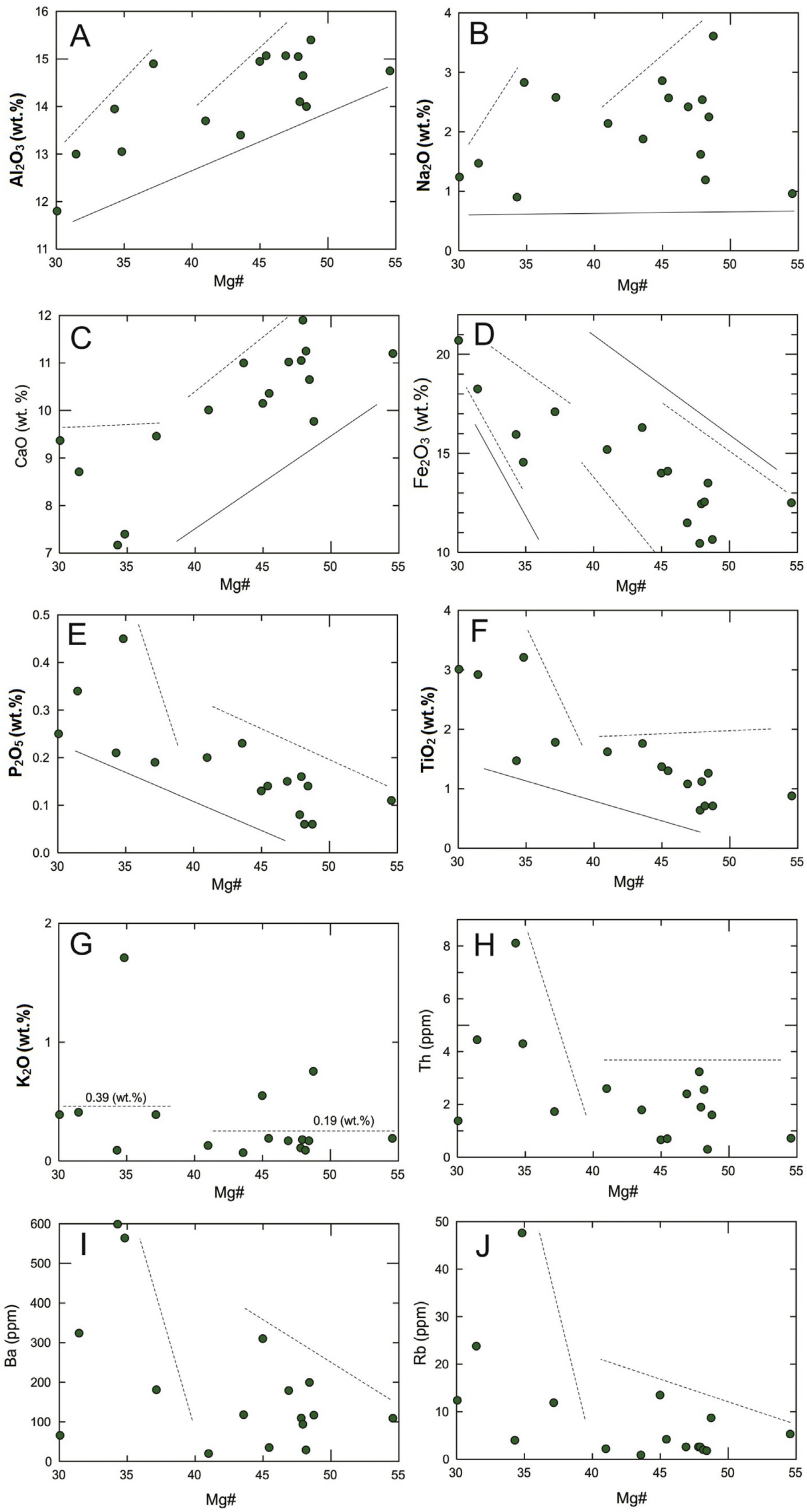

Fig. 5. Mg# vs. major and trace elements of Campo Grande amphibolites. Data from Table 1.

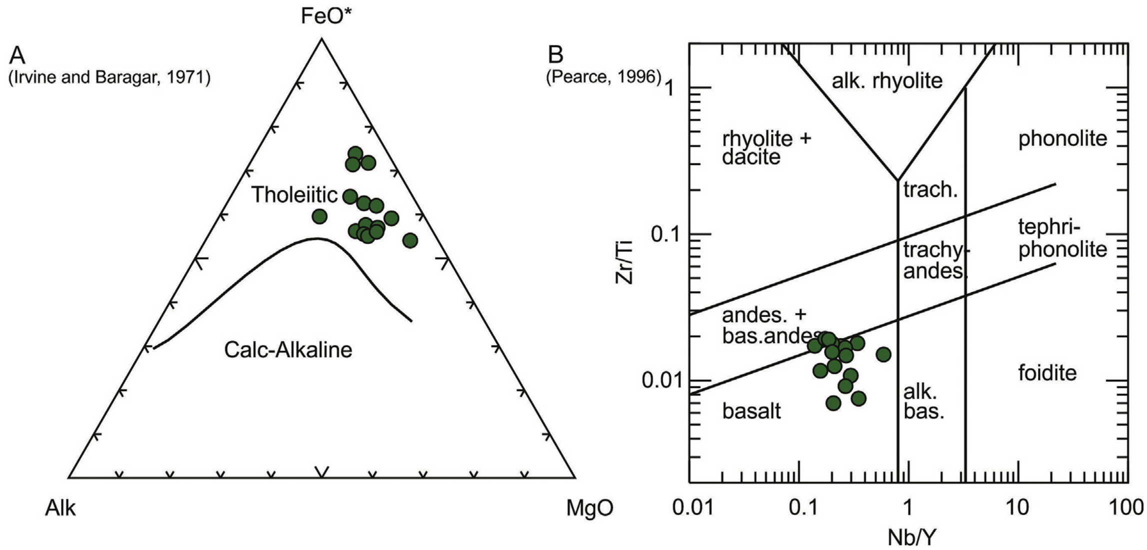

Fig. 6. (A) AFM diagram (after Irvine and Baragar, 1971) and (B) Zr/Ti vs. Nb/Y (after Pearce, 1996) plot for Campo Grande amphibolite samples. Data from Table 1.

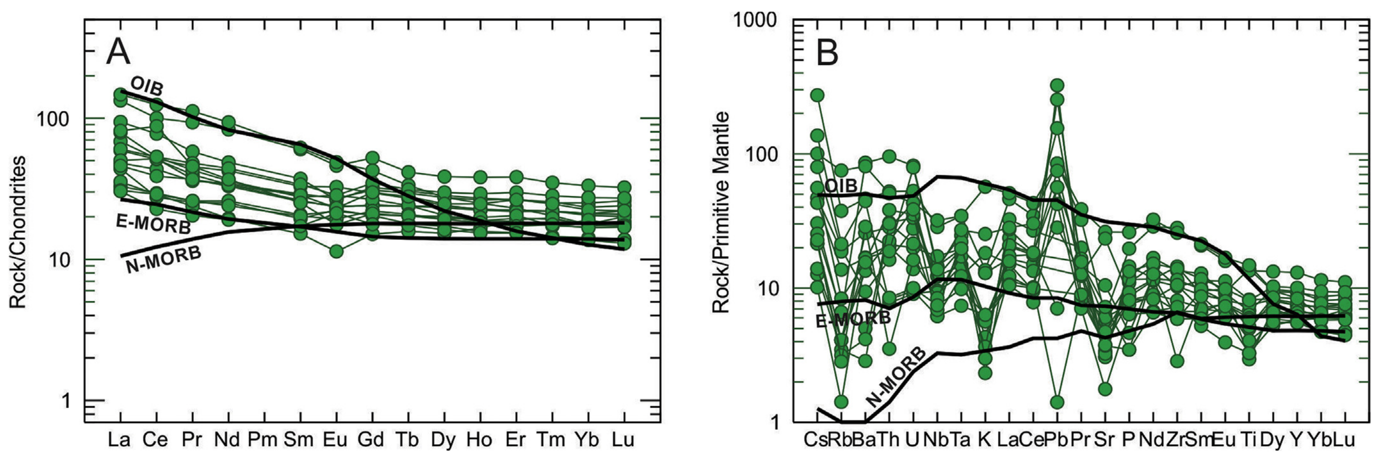

Fig. 7. (A–B) Chondrite normalized REE and primitive mantle (after Sun and McDonough, 1989) normalized trace element pattern for the Campo Grande amphibolite samples (data from Table 1). Samples with higher Mg# show a similar pattern to fractionated E-MORB, whereas amphibolites with lower Mg# have a similar pattern to ocean island basalts (OIB).

high-pressure mafic rocks. These amphibolites contain two zircon populations, one represented by elongated (between 100 μm and 200 μm in length), euhedral to subhedral crystals, and the other by well-rounded grains (50–100 μm across) (Fig. 9A–I). Cathodoluminescence and backscattered electrons imaging reveals zoned cores that are surrounded by high luminescent rims (prismatic habit) and homogeneous crystals (rounded shapes) of amphibolite zircon crystals (Fig. 9A–I). On the other hand, the host migmatite sample only contains oscillatory-zoned prismatic grains (100–300 μm) (Fig. 9G).

4.3.1. Amphibolite ADE-29

Collected at the western limit of the mapped mafic lenses (Fig. 2), the amphibolite sample ADE-29 has well-rounded (40–50 μm) zircon grains surrounded by high luminescent rims with Th/U ratios ranging between 0.116 and 0.587. These zircon grains display a U–Pb discordia age of 2663 ± 16 Ma (Fig. 10A), that we interpreted as the crystallization age of the mafic protolith. An inherited component is given by four prismatic (100–150 μm) zircon grains from this amphibolite, providing the age of 2992 ± 17 Ma (Fig. 10A). These Mesoarchean zircon grains show high luminescent rims (Fig. 9A) and Th/U ratios between 0.412 and 0.842. A metamorphic Neoproterozoic age (589 ± 13 Ma; $^{206}Pb/^{238}U$ age), was obtained on a subhedral (~150 μm) zircon core with low Th/U ratio of 0.002.

4.3.2. Amphibolite ADE-16

The amphibolite sample ADE-16, located in the central portion of the area, displays a U–Pb discordia age of 2657 ± 14 Ma (Fig. 10B). The zircon grains are subhedral (~50 μm) and have Th/U ratios of 0.121–0.326. One Mesoarchean age of 3007 ± 25 Ma ($^{207}Pb/^{206}Pb$ age) was obtained on an inherited prismatic (~100 μm) zircon core with the highest Th/U ratio (0.461). This sample presents a similar evolution to that recorded in sample ADE-29, but without the registration of Neoproterozoic metamorphic zircon.

4.3.3. Amphibolite ADE-20

The amphibolite sample ADE-20 shows a single group of zircon grains (Fig. 9C), yielding a Neoproterozoic concordia age of 605 ± 6 Ma (Fig. 10C) in well-rounded (~50 μm) zircon crystals that exhibit low Th/U ratios, ranging from 0.005 to 0.084.

4.3.4. Amphibolite AP-17

The amphibolite sample AP-17 displays an Archean age of 2675 ± 21 Ma and concordant zircon grains at the lower intercept, near 600 Ma (Fig. 10D). The latter subpopulation yields two concordia ages of 606 ±

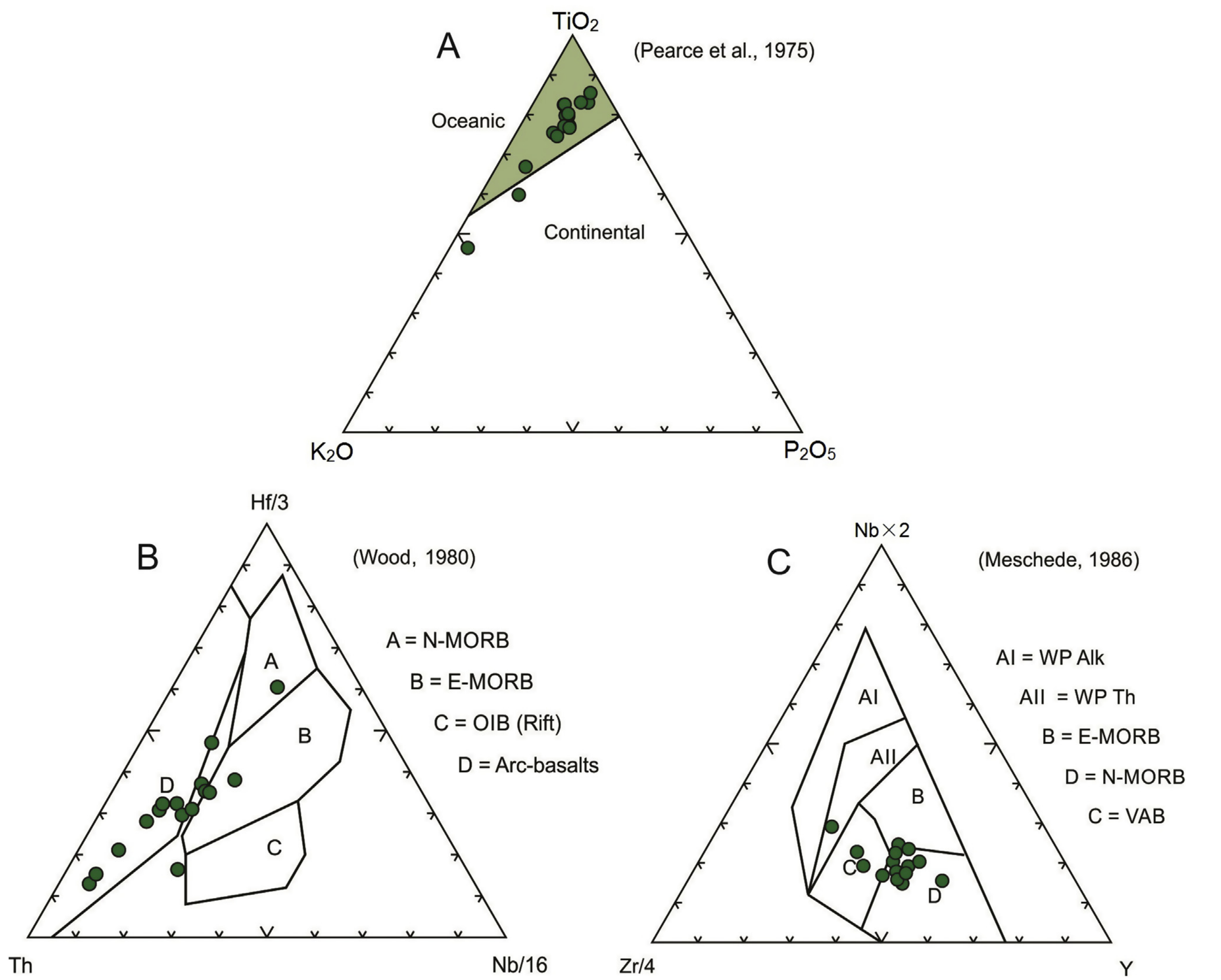

Fig. 8. (A) TiO_2–K_2O–P_2O_5 discriminant diagram (after Pearce el al., 1975). (B) Hf/3–Nb/16–Th ternary discrimination diagram (after Wood, 1980) and (C) Nb × 2–Zr/4–Y discriminant diagram (after Meschede, 1986) for Campo Grande amphibolites. Legend of Fig. 8C: VAB–volcanic arc basalts, WPAlk–within-plate alkali basalts and WPTh–within-plate tholeiite.

3 Ma and 623 ± 3 Ma (Fig. 10D), indicating progression of metamorphic ages with weighted mean concordia age of 614 ± 10 Ma. All Neoproterozoic zircon grains are rounded, do not show internal zonation (Fig. 9C and D), and have Th/U ratio from 0.009 to 0.050.

4.3.5. Amphibolite ADE-24A

The amphibolite sample ADE-24A, located in the central area, is unique in that it defines a Paleoproterozoic discordia age of 2023 ± 30 Ma (Fig. 10E), with concordant analyses between 2019 ± 28 Ma and 1961 ± 31 Ma, and a concordia age at 2005 ± 8 Ma (Fig. 10E). The zircon analyses show low Th/U ratio between 0.004 and 0.078. These Paleoproterozoic zircon crystals are well-rounded (100–200 μm) with unzoned cores followed by CL-dark inner rim and outermost CL-bright overgrowths (Fig. 9E) possibly due to a subsequent event. The narrowness of these zircon rims overgrowth prevented dating attempts. The Paleoproterozoic age obtained is taken as the record of a metamorphic event at ca. 2.0 Ga.

4.3.6. Amphibolite ADE-09

Sample ADE-09 relays a more complex history, with three zircon populations displaying different discordia ages (Fig. 10F), reflecting polycyclic deformation in the area. The Neoarchean age of 2692 ± 13 Ma is taken as the crystallization age of the amphibolite protolith. The Paleoproterozoic age of 1986 ± 21 Ma and the Neoproterozoic concordia age of 592 ± 5 Ma represent metamorphic events (Fig. 10F). Neoarchean zircon grains are well rounded (~50 μm) (Fig. 9F) with Th/U ratio between 0.147 and 0.323. The concordant Paleoproterozoic zircon is represented by rims of prismatic grains (~200 μm), and displays Th/U ratio between 0.011 and 0.162. Neoproterozoic zircon grains are rounded (~100 μm) and show the lowest Th/U ratios (0.001–0.003).

4.3.7. Host migmatite ADE-10

The sample ADE-10 was collected in the tonalitic paleosome (Fig. 4B) interpreted as portion of the migmatite that underwent zero partial melting. All zircon crystals are prismatic (100–300 μm), with Th/U ratios from 0.125 to 0.583 and internal zonation (Fig. 9G), typical magmatic crystal features (e.g. Corfu et al., 2003). Their analyses define a discordia age of 2923 ± 14 Ma (Fig. 11) with a concordant age of 2921 ± 16 Ma, interpreted as the crystallization age of the precursor magmatic source, i.e., before it was migmatized.

4.4. Lu–Hf isotope

19 analyzed zircon grains from five amphibolite samples were chosen for Lu–Hf isotope analyses (Table 2, Fig. 12A and B). The Mesoarchean zircon cores of ~3000 Ma yield low initial $^{176}Hf/^{177}Hf_{(t)}$ ratios of

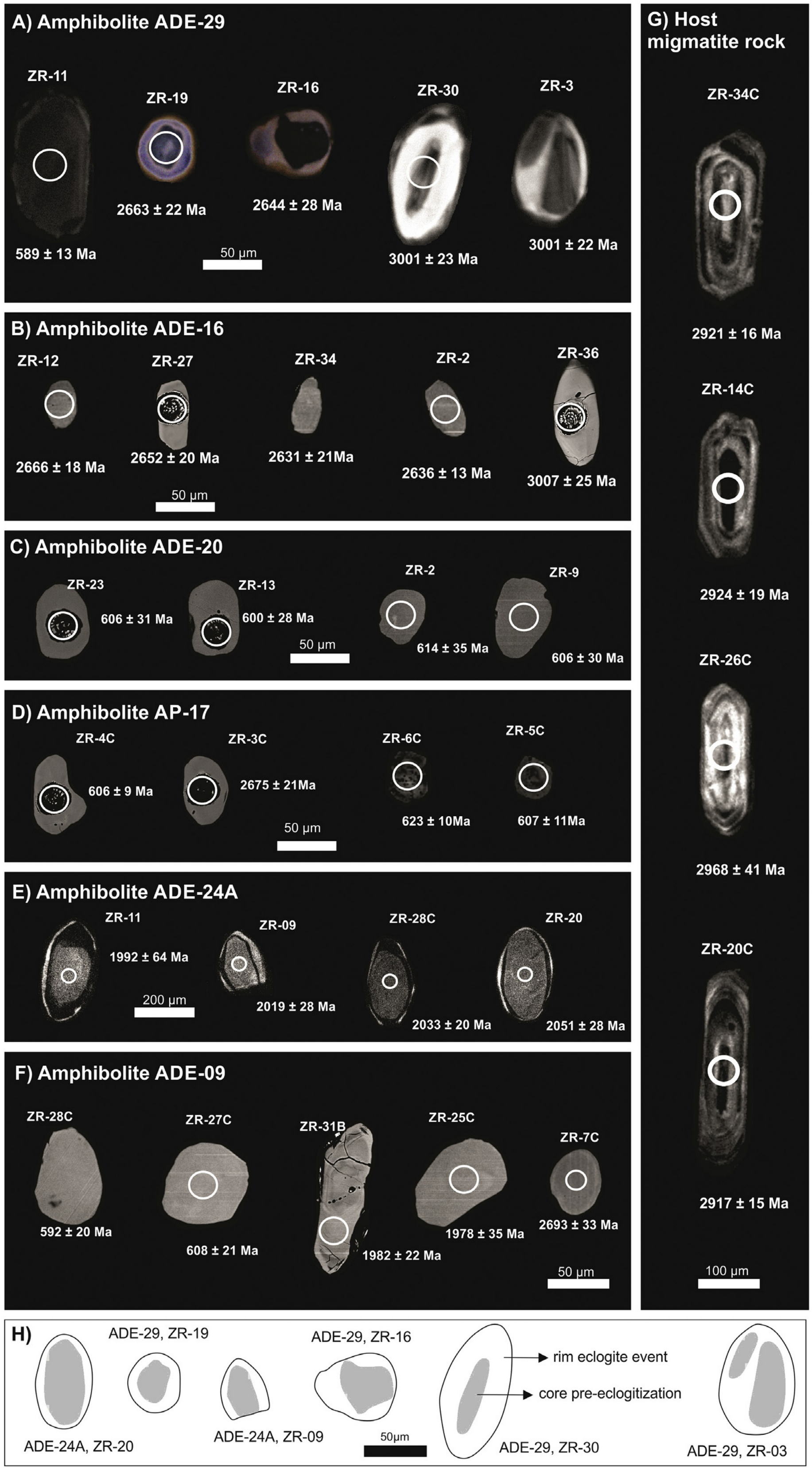

Fig. 9. (A to G) Representative CL (A, E and G) and BSE (B, C, D and F) images of zircon grains from amphibolite lenses and host migmatite from the Campo Grande area. The $^{207}Pb/^{206}Pb$ (>1.0 Ga) and $^{206}Pb/^{238}U$ (<1.0 Ga) ages are in Ma. (H) Schematic model of different domains of zircon from center to rim show inherited core followed by CL-bright oscillatory zoned rim. Amphibolite zircon core followed by CL-dark inner rim with oscillatory banding with outermost thin CL-bright rim.

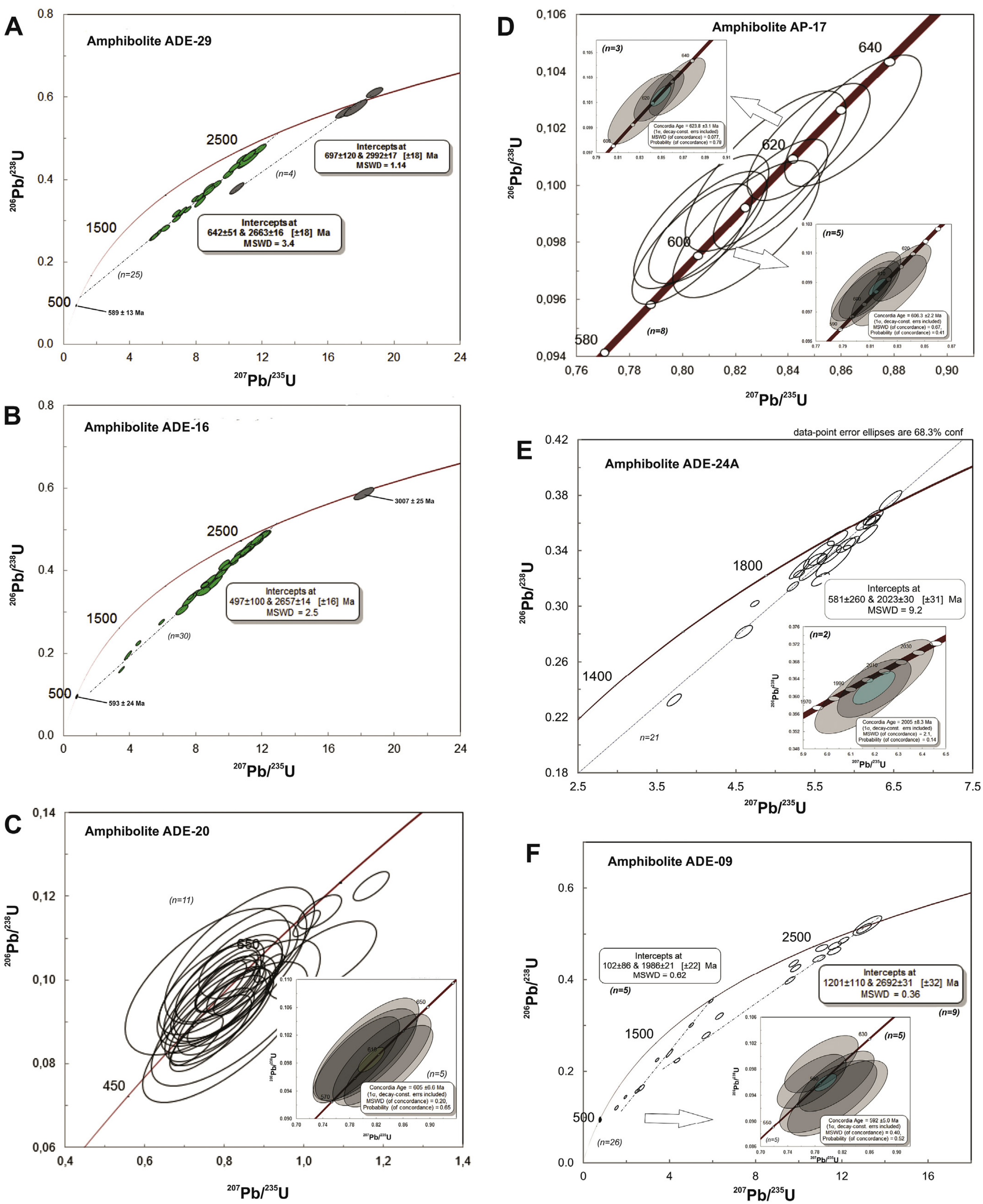

Fig. 10. Concordia diagrams of U–Pb zircon data of amphibolite samples. Data from Supplementary Table 2.

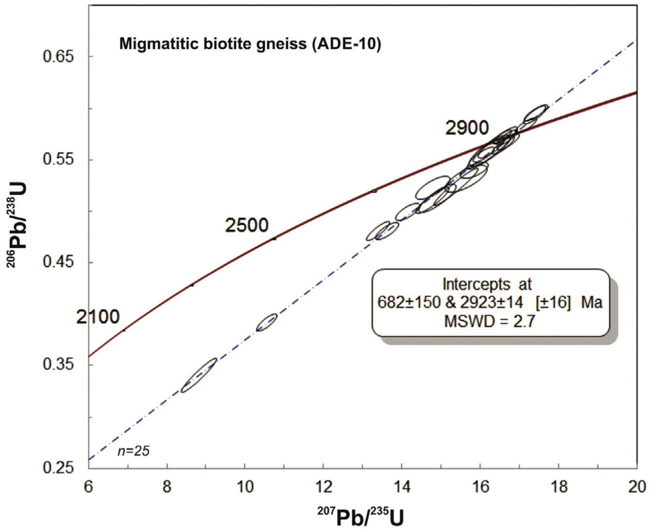

Fig. 11. Concordia diagram of U–Pb zircon data from host migmatitic biotite gneiss. Data from Supplementary Table 2.

0.280998–0.281280, and positive $\varepsilon_{Hf}(t)$ values of +5.4 to +15.3, with T_{DM} model ages of 2.65–3.02 Ga. On the other hand, Neoarchean zircon grains of 2693 Ma to 2633 Ma show heterogeneous Hf composition with high $^{176}Hf/^{177}Hf$ ratios of 0.281199–0.281926, with positive $\varepsilon_{Hf}(t)$ values of +3.8 to +30.6, and T_{DM} values of 1.78–2.76 Ga. The T_{DM} ages are less than the U–Pb crystallization age due to $\varepsilon_{Hf}(t)$ plotted above the fractionated depleted mantle. The Lu–Hf Isotope analyses show Pb loss, forming a horizontal distribution line, indicating that they are most likely derived from the $^{176}Hf/^{177}Hf$ isotopic system of 2.65 Ga (Fig. 12A). The Neoproterozoic zircon grains of 623–576 Ma yield initial $^{176}Hf/^{177}Hf_{(t)}$ ratios of 0.281586–0.282478 and $\varepsilon_{Hf}(t)$ values of +1.98 to –28.9 for the core and rim with younger T_{DM} Hf model ages of 1.1–2.2 Ga. There is an increase over time in the difference between the $^{176}Hf/^{177}Hf$ ratios of the 2.65 Ga igneous protolith and the Neoproterozoic metamorphism. The Neoproterozoic ZR-02 and ZR-06 zircon grains from sample AP-17 have lower $^{176}Hf/^{177}Hf_{(t)}$ ratios (0.280531–0.280583) and strong negative ε_{Hf} values (–64.6 and –65.8). However, these zircon crystals were affected by alteration and dissolution (Fig. 9D). In spite of metamict cores, they still preserve Neoproterozoic metamorphic age. Such T_{DM} model ages from the magmatic zircon grains indicate 1.8–2.7 Ga crustal residence time for the amphibolite lenses.

4.5. Sm–Nd isotope

T_{DM} model ages and $\varepsilon_{Nd}(t)$ of thirteen whole rock samples suggest a complex history for the amphibolites (Table 3, Fig. 13). The amphibolites display two Nd isotopic groups (G1 and G2) based on T_{DM} model ages older and younger than 2.6 Ga, the crystallization age of the mafic protolith. In G1, four samples (ADE-24A, ADE-16, AT-14 and AT-16) have negative ε_{Nd}(2.65 Ma) values (−1.03 to −7.97) and older T_{DM} model ages, between 3.7 Ga and 3.3 Ga; in this group, sample AP-10 has a less negative ε_{Nd}(2.6 Ma) value (–1.12) and a younger T_{DM} age of 3.19 Ga. The second group, G2, shows positive ε_{Nd}(2.6 Ma) values (+1.97 to +8.17), with younger T_{DM} model ages of 1.95–2.65 Ga. Nd isotopic data obtained for the host tonalitic paleosome restite? (sample ADE-10) shows T_{DM} model age of 3.2 Ga, with negative ε_{Nd}(2.9 Ma) = –2.58 (Table 3, Fig. 13).

ε_{Nd}(2.6 Ma) plotted against 1/Nd and $^{147}Sm/^{144}Nd$ shows the evolution and the distinction between amphibolites with different Nd isotopic signatures (Group 2) and preserved Nd Isotopic system (Group 1) (Fig. 14A and B). T_{DM} model age vs. 1/Nd and $^{147}Sm/^{144}Nd$ diagrams also separate G1 and G2 amphibolite samples (Fig. 14C and D). The samples of the G2 group have higher Mg# and modal concentration of

Table 2
LA-MC-ICPMS Lu–Hf isotopes from the Campo Grande amphibolite.

Sample	Zircon	U-Pb age (Ma)	CHUR	DM	Sample (present-day ratios)				Sample (initial ratios)			Crust Model Ages (Ga)		T_{DM} (Hf)
			$^{176}Hf/^{177}Hf(t)$	$^{176}Hf/^{177}Hf(t)$	$^{176}Hf/^{177}Hf$	±2SE	$^{176}Lu/^{177}Hf$	±2SE	$^{176}Hf/^{177}Hf_{(t)}$	$\varepsilon_{Hf}(t)$	±2SE	Mafic	Felsic	(Ga)
ADE-16	ZR29	593	0.282411	0.282818	0.281814	0.000025	0.000763	0.000026	0.281806	-21.43	1.61	3.73	2.44	1.98
	ZR36	3007	0.280845	0.281009	0.281057	0.000029	0.001014	0.000005	0.280998	5.47	0.07	3.04	3.03	3.02
ADE-29	ZR9	2633	0.281092	0.281295	0.281221	0.000344	0.000433	0.000019	0.281199	3.81	0.20	2.94	2.81	2.76
	ZR11	588	0.282414	0.282822	0.282023	0.000030	0.000742	0.000020	0.282014	-14.16	0.70	3.10	2.07	1.70
	ZR30	3001	0.280849	0.281014	0.281310	0.000029	0.000523	0.000040	0.281280	15.35	1.29	2.15	2.50	2.65
ADE-20	ZR3	610	0.282400	0.282806	0.282393	0.001102	0.000012	0.000002	0.282392	-0.27	0.07	1.91	1.37	1.17
	ZR9	606	0.282403	0.282809	0.282098	0.000105	0.000006	0.000001	0.282098	-10.78	1.82	2.82	1.91	1.57
	ZR18	710	0.282337	0.282732	0.282277	0.000088	0.000021	0.000002	0.282277	-2.12	0.21	2.14	1.55	1.33
ADE-09	ZR2C	2693	0.281052	0.281249	0.281263	0.000077	0.000447	0.000014	0.281240	6.67	0.37	2.72	2.71	2.71
	ZR7C	2693	0.281052	0.281249	0.281708	0.000151	0.000466	0.000014	0.281684	22.47	0.97	1.29	1.88	2.11
	ZR29C	2655	0.281078	0.281278	0.281922	0.000224	0.000339	0.000005	0.281905	29.44	0.72	0.62	1.48	1.82
	ZR10C	578	0.282420	0.282829	0.282385	0.000022	0.000018	0.000000	0.282385	-1.25	0.08	1.97	1.40	1.18
	ZR12C	592	0.282412	0.282819	0.282433	0.000110	0.000025	0.000001	0.282433	0.74	0.07	1.81	1.31	1.12
	ZR14C	2674	0.281065	0.281264	0.281389	0.000059	0.000523	0.000021	0.281362	10.58	0.60	2.36	2.49	2.54
	ZR15C	576	0.282422	0.282830	0.282478	0.000043	0.000016	0.000001	0.282478	1.98	0.27	1.69	1.23	1.06
AP-17	ZR2	602	0.282405	0.282811	0.280583	0.001610	0.000053	0.000006	0.280583	-64.54	9.42	7.27	4.59	3.56
	ZR3	2675	0.281064	0.281263	0.281960	0.000484	0.000652	0.000023	0.281926	30.67	1.39	0.52	1.43	1.78
	ZR4	606	0.282403	0.282809	0.281586	0.000241	0.000042	0.000002	0.281586	-28.93	1.66	4.37	2.83	2.25
	ZR6	623	0.282392	0.282796	0.280534	0.000969	0.000182	0.000009	0.280531	-65.88	4.61	7.40	4.68	3.64

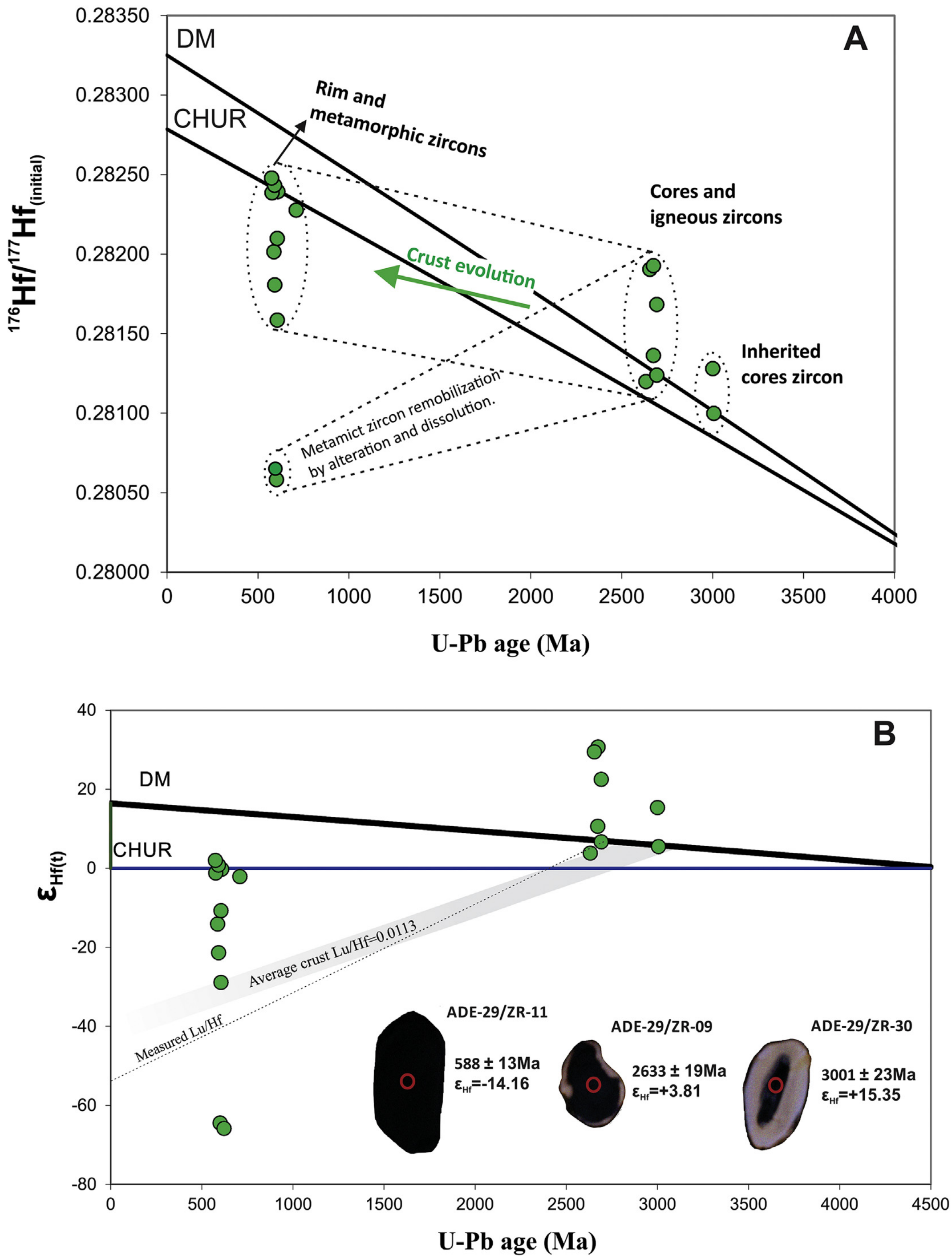

Fig. 12. Integrated zircon Lu–Hf isotope diagrams from the amphibolites samples. (A) Initial $^{176}Hf/^{177}Hf_{(t)}$ value and (B) $\varepsilon_{Hf}(t)$ vs. age, including CL images of zircon grains with analyzed spots for $^{207}Pb/^{206}Pb$ age and $\varepsilon_{Hf}(t)$. Data from Table 2.

garnet and pyroxene, with well-developed symplectitic texture, whereas the samples of the G1 group show lower Mg# and consist mainly of granoblastic amphiboles. Thus, we suggest that the more negative values of ε_{Nd}(2.65 Ga) and anomalously high T_{DM} for the G1 group (Fig. 13) are due to mantle enrichment processes.

5. Discussion

5.1. Origin of amphibolites

The studied amphibolites have basaltic composition, displaying sub-alkaline character and tholeiitic affinity (Fig. 6A and B), which is typical of basaltic melts in oceanic ridges or in supra-subduction zones (e.g. Pearce, 2008). The studied tholeiitic samples from the Campo Grande area display two different oceanic signatures, varying from E-MORB to OIB types in the Th/Yb vs. Nb/Yb and TiO_2/Yb vs. Nb/Yb discriminant diagrams (Fig. 15) (Pearce, 2008).

The Th–Nb proxy demonstrates volcanic arc affinity and oceanic subduction setting (Fig. 15A). The amphibolite samples are displaced above the MORB–OIB trend, similar to basaltic melts in subduction zones, while all oceanic basalts lie within a diagonal MORB–OIB array (Pearce, 2008). The Ti–Yb proxy is used to indicate melting depth,

Table 3
Sm–Nd isotopic data for the Campo Grande amphibolite and host migmatite gneiss.

Sample	Rock	Sm (ppm)	Nd (ppm)	$^{147}Sm/^{144}Nd$	$^{143}Nd/^{144}Nd \pm 2SE$	$\varepsilon_{Nd}(0)$	$\varepsilon_{Nd}(t)$	T_{DM} (Ga)
ADE-29	Amph (G2)	3.57	12.7	0.17	0.512416±13	–4.32	4.63	2.17
ADE-09		3.30	12.74	0.1566	0.512121±3	–10.09	3.32	2.46
ADE-20		2.23	9.5	0.1419	0.512116±5	–10.18	8.17	1.95
ADE-24B		4.24	16.43	0.156	0.512077±2	–10.95	2.66	2.55
AT-16		5.33	20.7	0.1558	0.512099±12	–10.51	3.17	2.48
AT-10		5.9	24.52	0.1454	0.511922±19	–13.97	3.18	2.5
AT-32		3.98	14.95	0.1609	0.512125±15	-10.00	1.97	2.65
AP-17		9.59	39.15	0.148	0.512104±3	–10.42	5.88	2.17
AP-10	Amph (G1)	5.31	19.65	0.1634	0.512011±4	–12.23	–1.12	3.19
AT-26		3.59	12.53	0.1734	0.512187±12	–8.8	–1.03	3.34
AT-14		4.44	19.77	0.1358	0.511189±4	–28.27	–7.97	3.69
ADE-16		4.33	16.94	0.1545	0.511773±8	–16.87	–2.81	3.33
ADE–24A		4.5	16.93	0.1607	0.511780±20	–16.74	–4.76	3.75
ADE-10	Host	5.55	33.2	0.1011	0.510677±8	–38.25	–2.58	3.22

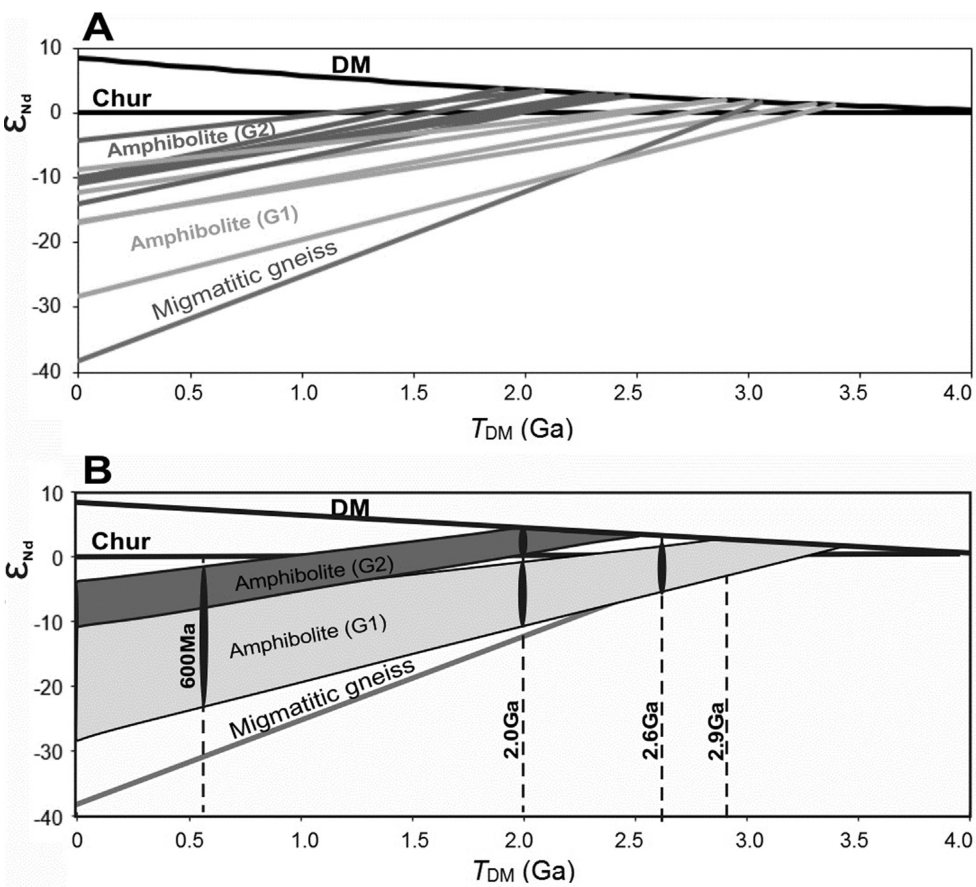

Fig. 13. Nd isotope compositions of amphibolites and host migmatitic gneiss samples. Data from Table 3.

mantle temperature and the thickness of the conductive lithosphere (Pearce, 2008). The TiO_2/Yb vs. Nb/Yb diagram shows that the amphibolite samples with MORB signature were generated at shallow-melting setting, while samples with OIB signature indicate deep-melting setting (Fig. 15B). In the Hf/Ta vs. Zr/Nb plot, mafic samples define an approximately linear distribution (Fig. 15C), as expected for oceanic basalts (Jochum et al., 1986), with similar evolution from primitive mantle to E-MORB. In this diagram, the analyzed samples display a larger enrichment pattern than reference values, supporting an enriched mantle source or continental assimilation of Zr and Hf. This latter hypothesis is evidenced by the presence of inherited zircon cores of 3.0–2.9 Ga, possibly from the host migmatite. Low Th/La ratios between 0.10 and 0.20 (Fig. 15D) are also consistent with oceanic basalts (Plank, 2005) and a source similar to the primitive mantle (~0.11; Sun and McDonough, 1989). High Th/La (~0.2) indicates an enriched source due to the preferential partitioning of La over Th in mafic and accessory minerals within the mantle (e.g. Rudnick and Gao, 2003; Plank, 2005).

Subsequent metasomatism of the amphibolite protoliths can be observed in Nb/Ta, La/Sm and Y/Ho ratios. These elements exhibit extremely coherent behavior during magmatic processes (e.g. Bau, 1996; Bau and Dulski, 1999). Therefore, disturbances in these ratios indicate hybridization processes with an enriched component (e.g. Pearce, 2008; Zhang et al., 2013; Wang et al., 2019). Enrichment of Ta relative to Nb (Fig. 16A) and enrichment in HREE (Fig. 16B) reflect the partitioning process within the crust-mantle system (e.g. Green, 1995). Despite the uniform Y/Ho ratio, increase in the absolute concentration of Y is

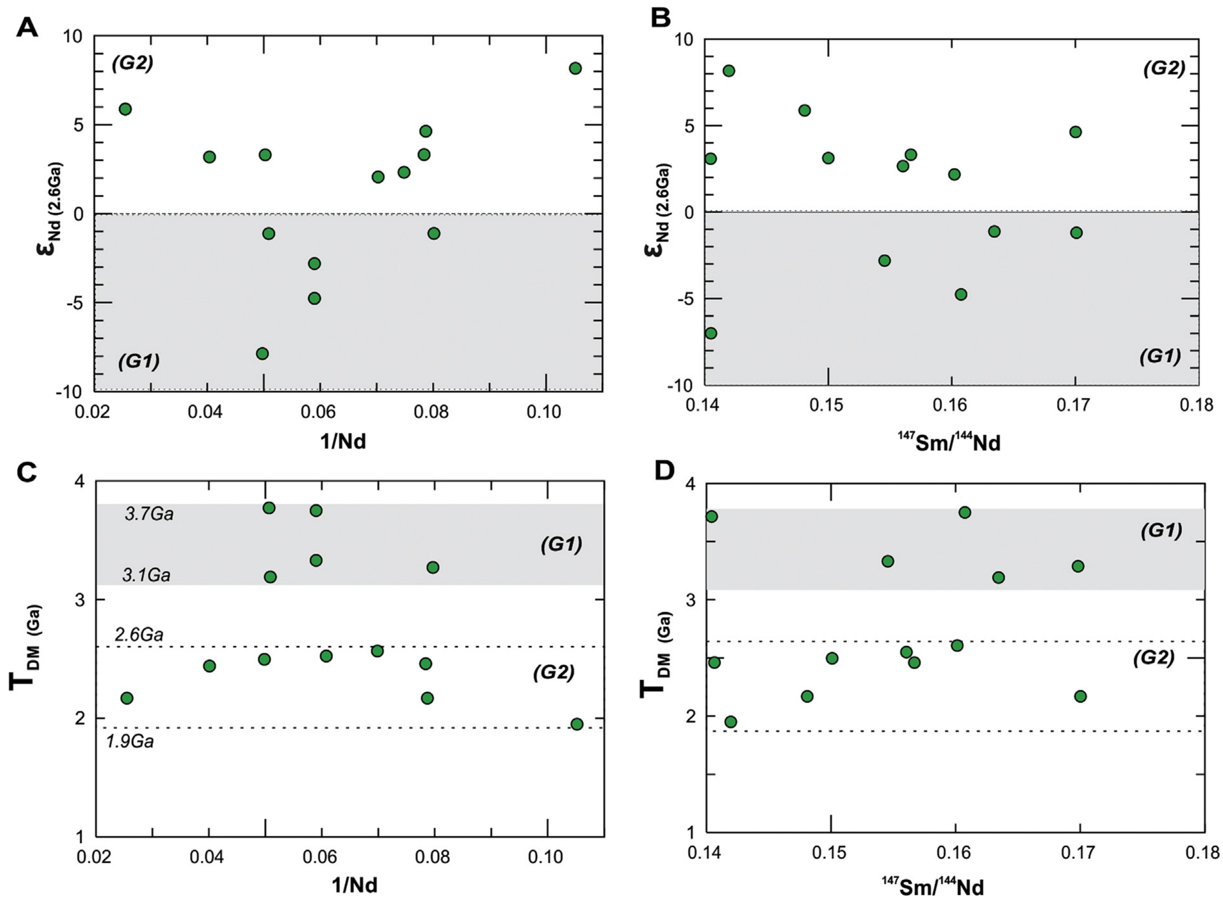

Fig. 14. (A–B) $\varepsilon_{Nd}(t)$ vs. 1/Nd and $^{147}Sm/^{144}Nd$ ratios. (C–D) T_{DM} model age vs. 1/Nd and $^{147}Sm/^{144}Nd$ ratios for Campo Grande amphibolites.

observed (25–45 ppm, Fig. 16C), while Y/Ho ratios show little variation (29–26), indicating non-CHARAC (CHArge-and-RAdius-Controlled) trace element behavior, possibly due to silicate melts or aqueous fluids (e.g. Bau, 1996). The amphibolite samples display decreasing Nb/Ta ratios from similar E-MORB compositions (~17.5) to more fractionated melts (~5), suggesting Ta enrichment in the oceanic protoliths, possibly during subduction.

The tectonic discriminant Ti–V diagram (Fig. 16D; Shervais, 1982) shows the typical subalkaline (tholeiitic) differentiation trend from arc-tholeiite to E-MORB. Strong Ti increase (0.4%–1.8%) is due to the very low partition coefficient of this element, almost always $<<1$ (Shervais, 1982). Depletion of V relative to Ti is a function of fO_2 of the magma and its source, the degree of partial melting and subsequent fractional crystallization (Shervais, 1982). Again, two groups are described, based on vanadium concentration. The first group shows values between 250 ppm and 350 ppm (MORB signature samples) and the second group displays V around 450 ppm (OIB signature samples).

The increase in incompatible elements, mainly Na, K, Ba, Ta, Ti, Th and LREE, can be attributed to the effect of mantle metasomatism, leading to a more plausible enriched source, previous to subduction (e.g. Willbold and Stracke, 2010; Huang et al., 2012; Kiseeva et al., 2016). Consequently, mafic to ultramafic oceanic crust enriched in incompatible elements implies that the mantle had already been strongly depleted at 2.65 Ga, as previously described in tholeiitic basalts enriched in Th and LREEs associated to subducted oceanic crust processes in the Archean of SW Greenland (Hawkesworth et al., 2010; Polat et al., 2011). The erratic and enriched pattern of the distribution of Zr, Hf and mainly Pb (Fig. 7B) is attributed to the assimilation of Archean zircon grains of the host migmatite during protolith crystallization, while changes in Sr, Ba and Nd patterns can be attributed to high-grade metamorphic processes (section 5.2). In summary, the geochemical data allow us to propose that the enriched amphibolite protoliths were crystallized at ca. 2.65 Ga in an oceanic crust with E-MORB and OIB signature.

A similar inference can be drawn from Hf and Nd isotopes. Hafnium compositions provide greater resolution in identifying discrete crust–mantle differentiation and the $\varepsilon_{Hf}(t)$ values are useful to identifying older crustal versus juvenile mantle components (e.g. Chauvel and Blichert-Toft, 2001; Hawkesworth and kemp, 2006; Zeh et al., 2007; Gerdes and Zeh, 2009). The $^{176}Hf/^{177}Hf_{(t)}$ ratios, $\varepsilon_{Hf}(t)$ and T_{DM} obtained in the analyzed rocks indicate that the amphibolite protoliths crystallized at 2.65 Ga from juvenile magma derived from sources with positive $\varepsilon_{Hf}(t)$ values of +3.81 to +30.66. Positive $\varepsilon_{Hf}(t)$ values support the preservation of the juvenile Archean oceanic crust in the Borborema Province. However, Nd isotopic data of these juvenile mafic rocks show negative ε_{Nd}(2.65 Ga) values (−1.03 to −7.976) and T_{DM} model ages of 3.7 Ga and 3.3 Ga, suggesting a component of metasomatism in the subcontinental lithospheric mantle, causing enrichment in the Sm–Nd isotopic system during Archean times. The group of mafic rocks with $T_{DM} = 1.95$–2.65 Ga (amphibolite G2) could represent a new juvenile magmatic event at 2.0 Ga with positive ε_{Nd}(2.0 Ga) (up to +5; Fig. 13B) due to ascent of asthenospheric mantle in an extensional exhumation process in the region at this time. Therefore, we have two hypotheses for 2.0 Ga amphibolite samples. These Paleoproterozoic ages represent the first high-grade metamorphic event in the 2.6 Ga protoliths due to the similar petrographic descriptions and geochemical fractionation pattern. All zircon analyses show Th/U $<$ 0.1 ratios and pervasive 2.0 Ga high-grade metamorphism in the Northeast Borborema Province (2.0 Ga in zircon rim; see Fig. 9F). In addition, 2.0 Ga eclogite conditions are recorded in Africa (e.g. François et al., 2018; Loose and Schenk, 2018) and Russia (e.g. Imayama et al., 2017). The other hypothesis is that they represent a new Paleoproterozoic tholeiitic magmatic pulse based on positive ε_{Nd}(2.0 Ga).

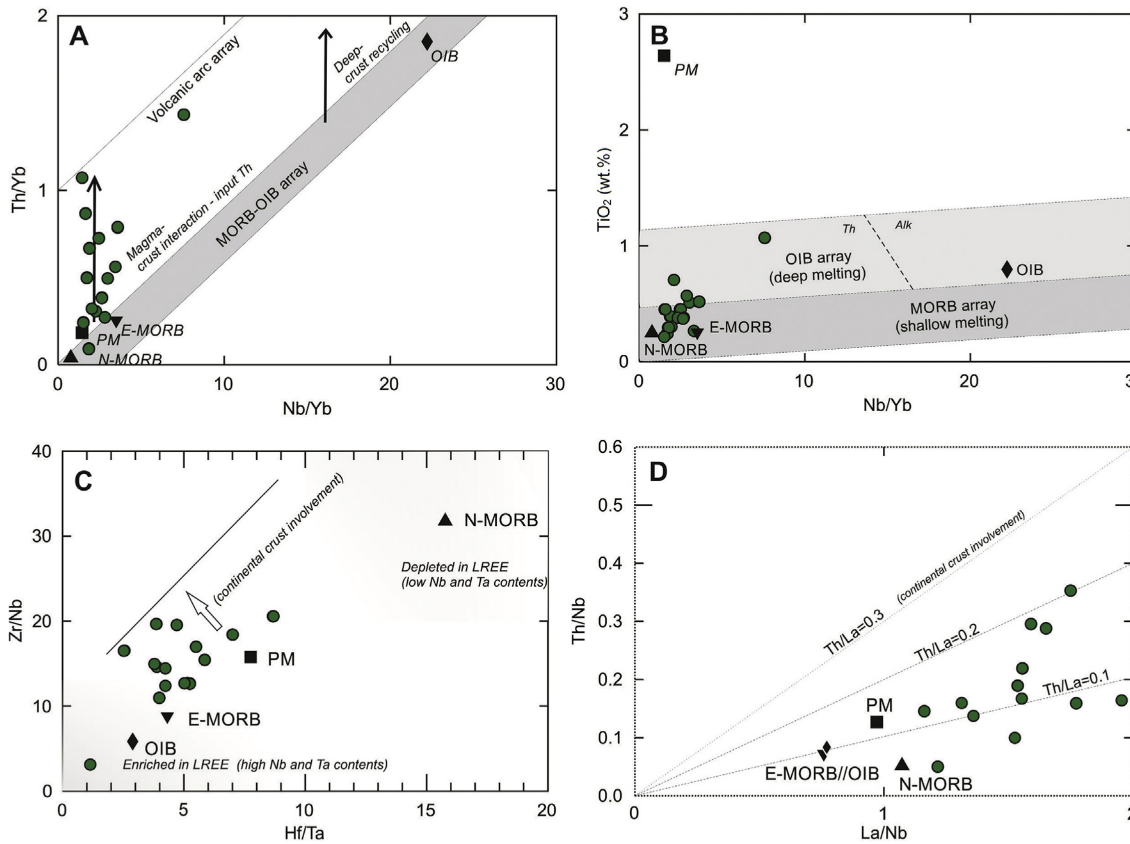

Fig. 15. (A) Th/Yb vs. Nb/Yb (after Pearce, 2008) for discrimination of oceanic basaltic rocks and (B) TiO_2 vs. Nb/Yb (after Pearce, 2008) discriminating between intra-oceanic settings of basaltic rocks formation. (C) Zr/Nb vs. Hf/Ta for source character identification (after Jochum et al., 1986). (D) Th/Nb vs. La/Nb (after Plank, 2005) for crustal contamination definition. Reference values for N-MORB, E-MORB, OIB and PM are from Sun and McDonough (1989).

5.2. Age of metamorphism and isotopic constraints

Several amphibolite lenses show the same age at around 2.65 Ga, interpreted as the age of crystallization of the protolith, based on internal zonation, morphology and high Th/U ratio in zircon cores. The presence of inherited zircon cores of 3.0–2.9 Ga indicates that the amphibolites represent tholeiitic magma emplaced into the Mesoarchean basement during extension. The Archean age at 2.9 Ga of the basement migmatite-gneiss suggests reworked Mesoarchean continental crust in this segment of the Rio Grande do Norte domain and shows the existence of an old block, not recognized previously in the regional context of the Borborema Province.

The age of metamorphic events in the region is still an open question. Zircon crystals are crucial to support interpretation of their ages in the context of the P-T history (e.g. Kohn et al., 2015). For new metamorphic zircon to form under high-grade metamorphism conditions, either the presence of a hydrous fluid or melt phase is required (e.g. Tichomirowa et al., 2005) or else via solid-state recrystallization (e.g. Rubatto et al., 2006). Several zircon grains analyzed in the amphibolite samples record evidence of the first metamorphic event of 2.0 Ga. These grains are rounded and unzoned, and generally have Th/U ratios <0.1 (Fig. 17), characteristics that are attributed to metamorphic zircon (e.g. Rubatto and Gebauer, 2000). However, it is known that metamorphic zircon in some high-grade rocks (e.g. granulite facies) displays Th/U ratios >0.1 (e.g. Korhonen et al., 2013). The higher Th/U ratios in zircon formed under granulite-eclogite facies conditions reflect both an increase in Th and a decrease in U contents (e.g. Yakymchuk and Brown, 2019). Thus, these ratios are controlled by other major or accessory mineral phases and their partitioning coefficient with zircon.

The internal textures of the Campo Grande amphibolite zircon grains are consistent with eclogite zircon (e.g. Corfu et al., 2003). These zircon crystals occur both in the matrix (symplectic texture) and as inclusions in different places within garnet porphyroblasts. They are subrounded and somewhat irregular and show relatively homogeneous internal textures (Fig. 9H). Retro-eclogites may contain complex zircon types: older homogeneous or growth zoned cores pre-dating eclogitization and metamorphic rims. The interfaces between irregular cores and rims are well-defined, showing either very fine or very coarse bands (Fig. 9H), and indicating resorption and recrystallization (e.g. Corfu et al., 2003). Our findings indicate that this is the case of analyzed zircon grains from Campo Grande mafic rocks.

The second metamorphic event at 600 Ma was more pervasive and is recorded in the majority of dated amphibolite lenses. The Neoproterozoic zircon grains, forming the youngest cluster of concordant analyses between 623 ± 3 Ma and 592 ± 5 Ma, display low Th/U ratios (<0.1; Fig. 17). As indicated by zircon rims in the Campo Grande mafic rocks, the high-grade metamorphic event resulted in negative $\varepsilon_{Hf}(t)$ values up to –65.88.

Theoretical models show that the time required to produce unzoned crystals of 2–3 mm size is in the order of 10–50 Ma (Caddick et al., 2010) for metamorphic temperatures around 690 °C. Furthermore, zircon is likely to grow under retrograde conditions when garnet is dissolved (e.g. Kohn et al., 2015; Tedeschi et al., 2017). Hence, the data suggest that the Campo Grande amphibolites experienced HP conditions for approximately 30 Ma (623–592 Ma). Therefore, we do not have the mineral assemblage to prove that Th/U ratios <0.1 are an unfailing indicator of metamorphic recrystallization. Symplectite texture formed through the reaction omphacite + H_2O → clinopyroxene + plagioclase + amphibole ± quartz is observed in these rocks and is considered as related to retrogressed mafic eclogites (e.g. Waters, 2003; Lanari et al., 2013; Tedeschi et al., 2017). We found this texture developed as coronae around garnet porphyroblasts in the studied rocks. The shape of the garnet crystals,

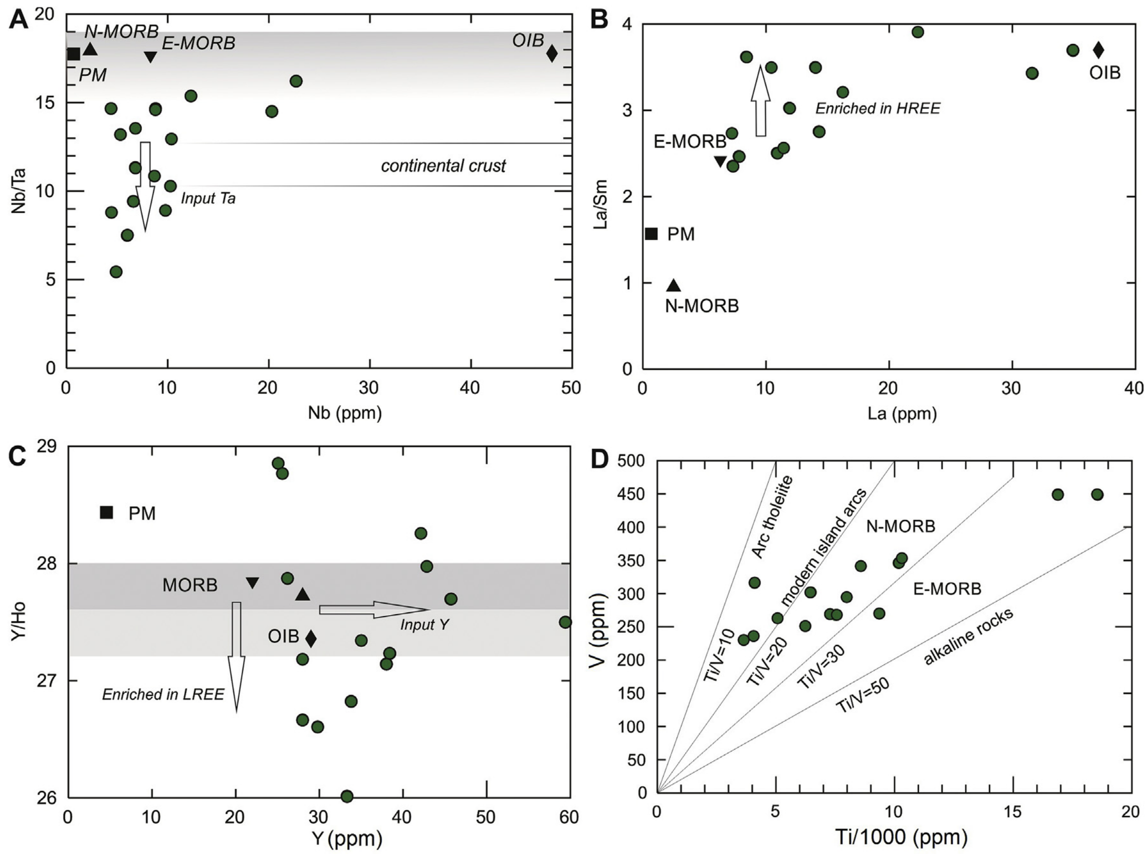

Fig. 16. Plots of (A) Nb/Ta vs. Nb, (B) La/Sm vs. La and (C) Y/Ho vs. Y for Campo Grande amphibolites. Compatible behavior during igneous processes increases from A to C. Reference values for N-MORB, E-MORB, OIB and PM are from Sun and McDonough (1989). (D) Vanadium vs. Ti/1000 variation diagram (after Shervais, 1982) for Campo Grande amphibolites.

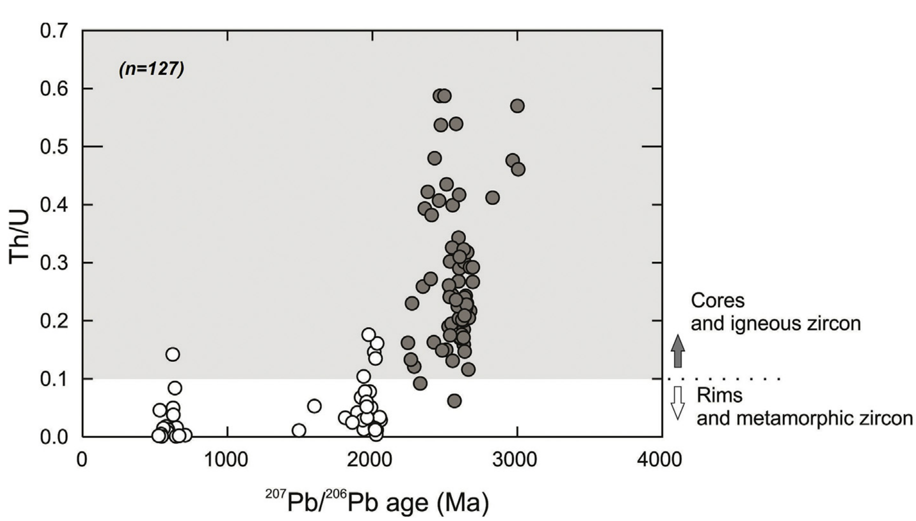

Fig. 17. Th/U ratio vs. $^{207}Pb/^{206}Pb$ ages from the Campo Grande amphibolite samples. Th/U ranges of 0.01–1.4 in magmatic cores and 0.01–0.1 in metamorphic rims and grains.

showing lobed edges, suggests resorption during the formation of the coronae (e.g. White et al., 2008; Lanari et al., 2017). Similar reactions have been observed in retrogressed mafic eclogites (e.g. Waters, 2003; Lanari et al., 2013) and in HP rocks (Tedeschi et al., 2017), corresponding to the amphibolite-eclogite facies transition (ca. 650–700 °C at 13–15 kbar), followed by near isothermal decompression.

Therefore, based on morphology, internal texture, Th/U ratios and combined U–Pb and Lu–Hf *in situ* analyses on zircon, we propose that the Campo Grande Block was generated from 2.9 Ga tonalitic and 2.65 Ga mafic magmatism. The magmatic protoliths were submitted to two high-grade metamorphic events at 2.0 Ga and 0.6 Ga. Therefore, the study area shows a complex polycyclic evolution (Fig. 18).

5.3. Implications for West Gondwana

High-pressure amphibolites of the Campo Grande area display

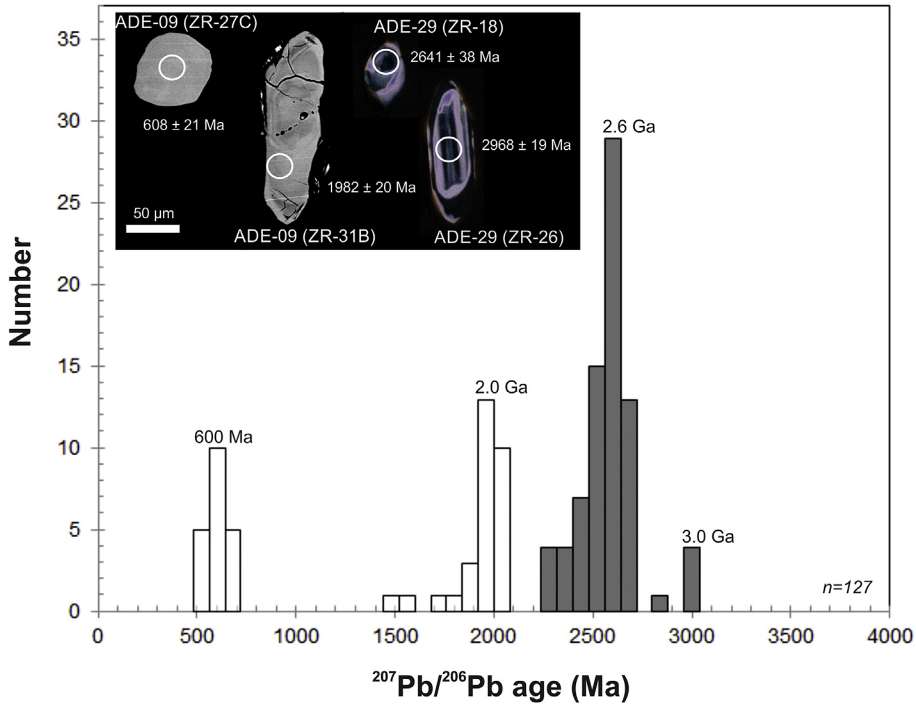

Fig. 18. Histogram of $^{207}Pb/^{206}Pb$ ages of the Campo Grande mafic rocks, including CL and BSE images of zircon grains with analyzed spots for $^{207}Pb/^{206}Pb$ (>1.0 Ga) and $^{206}Pb/^{238}U$ (<1.0 Ga) age. Data from Supplementary Table 2.

evidence of oceanic crust generation during the Archean in the Borborema Province. We interpret this assemblage as retro-eclogites that represent a different context in terms of temporal and petrogenetic correlation with other occurrences described in the Borborema Province and in other Brazilian provinces. In the Southern Brasília orogen, 620–588 Ma (U–Th)–Pb monazite ages from matrix-hosted patchy monazite are interpreted to date exhumation of HP rocks, as recorded by close-to-isothermal decompression, and subsequent close-to-isobaric cooling (Reno et al., 2012). The metamorphic peak for the Southern Brasília orogen was also dated around 630 Ma and retrogression conditions at 603 ± 7 Ma (Tedeschi et al., 2017). In the Borborema Province, the Santa Quitéria Magmatic arc (Fetter et al., 2003; Ganade et al., 2016) is associated to a collisional and high-grade metamorphic event dated at 640–620 Ma (Arthaud et al., 2008; Santos et al., 2008; Amaral et al., 2017). The 614.9 ± 7.9 Ma age of a metamafic rock, interpreted as retro-eclogite, records the minimum age of the high-grade metamorphic conditions (upper amphibolite/granulite facies) (Santos et al., 2009, 2015; Ganade et al., 2014).

The 630–590 Ma HP mafic rocks from the Borborema and Tocantins provinces suggest that the Pharusian and Goiás oceans were spatially linked during the amalgamation of West Gondwana (Santos et al., 2009; Reno et al., 2012; Ganade et al., 2016; Tedeschi et al., 2017). Therefore, all eclogite evidences described before in Brazil (e.g. Santos et al., 2009; Reno et al., 2012; Ganade et al., 2016; Tedeschi et al., 2017) are related to tectonic events affecting piles of metasedimentary rocks inside Neoproterozoic fold-and-thrust belts. Although similar Neoproterozoic ages were found in the Campo Grande high-pressure mafic rocks, they are associated to a basement inlier within the Neoproterozoic supracrustal sequences in the Borborema Province.

6. Conclusion

The main conclusions of this study are as follows:

(I) Amphibolites of the Campo Grande area, Rio Grande do Norte domain, Borborema Province, Northeast Brazil, display typical textures found in retro-eclogite, e.g. massive plagioclase-clinopyroxene symplectite between poikiloblastic garnet and granoblastic amphibole.

(II) Chondrite-normalized REE and trace elements suggest an enriched mantle source with E-MORB and OIB signature for the amphibolite protolith.

(III) Amphibolite samples have Archean crystallization age of 2.65 Ga and were metamorphosed at 2.0 Ga and 600 Ma. Analyzed samples contain inherited zircon grains of 2.9 Ga compatible with host migmatite gneiss zircon of 2923 ± 14 Ma.

(IV) Petrographic analysis and symplectite texture of the amphibolites suggest maximal conditions at the amphibolite/eclogite facies boundary, followed by near isothermal decompression related to orogenic collision stages between Archean and Paleoproterozoic terranes.

(V) The Campo Grande rock assemblage is composed of Archean units that were amalgamated to West Gondwana during crustal reworking associated to the Neoproterozoic Brasiliano/Pan-African orogeny.

(VI) The Campo Grande Block comprises tonalite magmatism at ca. 2.9 Ga, juvenile tholeiitic magmatism at ca. 2.65 Ga that formed the amphibolite protoliths, followed by high-grade metamorphic events at ca. 2.0 Ga and ca. 600 Ma.

Declaration of competing interest

The authors declare that they have no known competing financial interests or personal relationships that could have appeared to influence the work reported in this paper.

Acknowledgments

This study is part of the first author's PhD thesis in development at the Institute of Geosciences (Universidade de Brasília). The authors acknowledge the support of the INCT Estudos Tectônicos (CAPES/CNPq-465613/2014-4 and FAPDF-193.001.263/2017). ELD, TJSS, RAF and

MT acknowledge CNPq research fellowships.

Appendix A. Supplementary data

Supplementary data to this article can be found online at https://doi.org/10.1016/j.gsf.2020.03.004.

References

Albarède, F., Telouk, P., Blichert-Toft, J., Boyet, M., Agranier, A., Nelson, B., 2004. Precise and accurate isotopic measurements using multiple-collector ICPMS. Geochem. Cosmochim. Acta 68, 2725–2744.

Amaral, W.S., Kraus, R.K., Dantas, E.L., Fuck, R.A., Pitombeira, J.P.A., 2017. Sinistral reactivation of the transbrasiliano lineament: structural and geochronological evidences in the Cariré granulite zone, Borborema province - NE Brazil. J. S. Am. Earth Sci. 79, 409–420.

Archanjo, C.J., Viegas, L.G.F., Hollanda, M.H.B.M., Souza, L.C., Liu, D., 2013. Timing of the HT/LP transpression in the Neoproterozoic Seridó belt (Borborema Province, Brazil): Constraints from U-Pb (SHRIMP) geochronology and implications for the connections between NE Brazil and West Africa. Gondwana Res. 23, 701–714.

Arthaud, M.H., Caby, R., Fuck, R.A., Dantas, E.L., Parente, C.V., 2008. Geology of the northern Borborema province, NE Brazil and its correlation with Nigeria, NW Africa. In: Pankhurst, R.J., Trouw, R.A.J., Brito Neves, B.B., de Wit, M.J. (Eds.), West Gondwana: Pre-Cenozoic Correlation across the South Atlantic Region, vol. 294. Geological Society of London, pp. 49–67.

Bau, M., 1996. Controls on the fractionation of isovalent trace elements in magmatic and aqueous systems: evidence from Y/Ho, Zr/Hf, and lanthanide tetrad effect. Contrib. Mineral. Petrol. 123, 23–333.

Bau, M., Dulski, P., 1999. Comparing yttrium and rare earths in hydrothermal fluids from the Mid-Atlantic Ridge: implications for Y and REE behaviour during near-vent mixing and for the Y/Ho ratio of Proterozoic seawater. Chem. Geol. 155, 77–90.

Blichert-Toft, J., Albarède, F., 1997. The Lu-Hf isotope geochemistry of chondrites and the evolution of the mantle-crust system. Earth Planet Sci. Lett. 148, 243–258.

Brito Neves, B.B., 2011. The Paleoproterozoic in the South-American continent: diversity in the geologic time. J. S. Am. Earth Sci. 32, 270–286.

Brito Neves, B.B., Fuck, R.A., 2014. The basement of the South American platform: half Laurentian (N-NW) + half Gondwanan (E-SE) domains. Precambrian Res. 244, 75–86.

Brito Neves, B.B., Dos Santos, E.J., Van Schmus, W.R., 2000. Tectonic history of the Borborema province, northeastern Brazil. In: Cordani, U., Milani, E.J., Thomaz Filho, A., Campos, D.A. (Eds.), Tectonic Evolution of South America, 31st International Geological Congress. Rio de Janeiro, Brazil pp. 151–182.

Brown, M., 2009. Metamorphic Patterns in Orogenic Systems and the Geological Record, 318. Geol. Soc. Lond. Spec. Publ., pp. 37–74

Brown, M., 2014. The contribution of metamorphic petrology to understanding lithosphere evolution and geodynamics. Geosci. Front. 5, 553–569.

Bühn, B.M., Pimentel, M.M., Matteini, M., Dantas, E.L., 2009. High spatial resolution analyses of Pb and U isotopes for geochronology by laser ablation multi-collector inductively coupled plasma mass spectrometry LA-MC-ICP-MS. An Acad. Bras Ciências 81, 1–16. https://doi.org/10.1590/S0001-37652009000100011.

Caddick, M.J., Konopasek, J., Thompson, A.B., 2010. Preservation of garnet growth zoning and the duration of prograde metamorphism. J. Petrol. 51, 2327–2347.

Carswell, D.A., 1990. Eclogite Facies Rocks. Blackie and Son Ltd., Glasgow, London.

Chauvel, C., Blichert-Toft, J., 2001. A hafnium isotope and trace element perspective on melting of the depleted mantle. Earth Planet Sci. Lett. 190, 137–151.

Chu, N.C., Taylor, R.N., Chavagnac, V., Nesbitt, R.W., Boella, R.M., Milton, J.A., German, C.R., Bayon, G., Burton, K., 2002. Hf isotope ratio analysis using multicollector inductively coupled plasma mass spectrometry: an evaluation of isobaric interference corrections. J. Anal. Atomic Spectrom. 17, 1567–1574.

Corfu, F., Hanchar, J.M., Hoskin, P.O.W., Kinny, P., 2003. Atlas of zircon textures. In: Zircon, Hanchar, J.M., Hoskin, P.W.O. (Eds.), Reviews in Mineralogy & Geochemistry, vol. 53. Mineralogical Society of America and Geochemical Society, pp. 469–500.

Corsini, M., Vauchez, A., Archanjo, C., Jardim de Sá, E.F., 1991. Strain transfer at continental scale from a transcurrent shear zone to a transpressional fold belt: the Patos-Seridó system, northeastern Brazil. Geology 19, 586–589.

Dantas, E.L., Van Schmus, W.R., Hackspacher, P.C., Fetter, A.H., Neves, B.B.B., Cordani, U.G., Nutman, A.P., Williams, S., 2004. The 3.4-3.5 Ga São José do Campestre Massif, NE Brazil: remnants of the oldest crust in South America. Precambrian Res. 130, 113–137.

Dantas, E.L., Negrão, M.M., Buhn, B., 2008. 2.3 Ga continental crust generation in the Rio Grande do Norte terrane, NE-Brazil. In: 6th South American Symposium on Isotope Geology, p. 40. Abstract.

Defant, M.J., Drummond, M.S., 1990. Derivation of some modern arc magmas by melting of young subducted lithosphere. Nature 347, 662–665.

DePaolo, D.J., 1981. A neodymium and strontium isotopic study of the Mesozoic calc-alkaline granitic batholithys of the Sierra Nevada and Peninsular Ranges, California. J. Geophys. Res. 86, 10470–10488.

Ferreira, A.C.D., Ferreira Filho, C.F., Dantas, E.L., Souza, V.S., 2019. Paleoproterozoic mafic-ultramafic magmatism in the northern Borborema province, NE Brazil: tectonic setting and potential for deposits. J. Geol. 127, 483–504.

Fetter, A.H., Santos, T.J.S., Van Schmus, W.R., Hackspacher, P.C., Brito Neves, B.B., Arthaud, M.H., Nogueira Neto, J.A., Wernick, E., 2003. Evidence for Neoproterozoic continental arc magmatism in the Santa Quitéria Batholith of Ceará state, NW Borborema province, NE Brazil: implications for the assembly of West Gondwana. Gondwana Res. 6, 265–273.

François, C., Debaille, V., Paquette, J.-L., Baudet, D., Javaux, L.J., 2018. The earliest evidence for modern-style plate tectonics recorded by HP–LT metamorphism in the Paleoproterozoic of the Democratic Republic of the Congo. Sci. Rep. 8, 15452.

Galindo, A.C., 1993. Petrologia dos granitoides brasilianos da região de Caraúbas e Umarizal, oeste do Rio Grande do Norte. Tese (Doutorado) - Centro de Geociências, Universidade Federal do Pará, Natal, p. 370 (in Portuguese).

Ganade, C.E., Rubatto, D., Hermann, J., Cordani, U.G., Caby, R., Basei, M.A., 2014. Ediacaran 2,500-km-long synchronous deep continental subduction in the West Gondwana Orogen. Nat. Commun. 5, 5198.

Ganade, C.E., Cordani, U.G., Agbossoumounde, Y., Caby, R., Basei, M.A.S., Weinberg, R.F., Sato, K., 2016. Tightening-up NE Brazil and NW Africa connections: new U-Pb/Lu-Hf zircon data of a complete plate tectonic cycle in the Dahomey belt of the West Gondwana Orogen in Togo and Benin. Precambrian Res. 276, 24–42.

Gerdes, A., Zeh, A., 2009. Zircon formation versus zircon alteration - new insights from combined U-Pb and Lu-Hf in-situ LA-ICP-MS analyses, and consequences for the interpretation of Archean zircon from the Central Zone of the Limpopo Belt. Chem. Geol. 261, 230–243.

Gilotti, J.A., 2013. The realm of ultrahigh-pressure metamorphism. Elements 9, 255–260.

Gioia, S.M.C.L., Pimentel, M.M., 2000. The Sm-Nd isotopic method in the geochronology laboratory of the University of Brasília. An Acad. Bras Ciências 72, 219–245. https://doi.org/10.1590/S0001-37652000000200009.

Gordon, S.M., Whitney, D.L., Teyssier, C., Fossen, H., 2013. U–Pb dates and trace-element geochemistry of zircon from migmatite, Western Gneiss Region, Norway: significance for history of partial melting in continental subduction. Lithos 170–171, 35–53.

Gray, D.R., Foster, D.A., Meert, J.G., Goscombe, B.D., Armstrong, R., Trouw, R.A.J., Passchier, C.W., 2008. A Damara orogen perspective on the assembly of southwestern Gondwana. In: Pankhurst, R.J., Trouw, R.A.J., de Brito Neves, B.B., de Wit, M.J. (Eds.), West Gondwana: Pre-Cenozoic Correlations across the South Atlantic Region. Geol. Soc. Lond. Spec. Publ, 294, 257–278.

Green, T.H., 1995. Significance of Nb/Ta as an indicator of geochemical processes in the crust-mantle system. Chem. Geol. 20, 347–359.

Hawkesworth, C.J., Kemp, A.I.S., 2006. Using hafnium and oxygen isotopes in zircons to unravel the record of crustal evolution. Chem. Geol. 226, 144–162.

Hawkesworth, C.J., Dhuime, B., Pietranik, A.B., Cawood, P.A., Kemp, A.I.S., Storey, C.D., 2010. The generation and evolution of the continental crust. J. Geol. Soc. 167, 229–248.

Hills, D.V., Haggerty, S.E., 1989. Petrochemistry of eclogites from the Koidu Kimberlite complex. Sierra Leone. Contrib. Min. Pet. 103, 397–422.

Holder, R.M., Viete, D.R., Brown, M., Johnson, T.E., 2019. Metamorphism and the evolution of plate tectonics. Nature 572, 378–381.

Hollanda, M.H.B.M., Archanjo, C.J., Souza, L.C., Dunyi, L., Armstrong, L., 2011. Long-lived Paleoproterozoic granitic magmatism in the Seridó-Jaguaribe domain, Borborema province-NE Brazil. J. S. Am. Earth Sci. 32, 287–300.

Hollanda, M.H.B.M., Archanjo, C.J., Bautista, J.R., Souza, L.C., 2015. Detrital zircon ages and Nd isotope compositions of the Seridó and Lavras da Mangabeira basins (Borborema Province, NE Brazil): evidence for exhumation and recycling associated with a major shift in sedimentary provenance. Precambrian Res. 258, 186–207.

Huang, J.X., Gréau, Y., Griffin, W.L., O'Reilly, S.Y., Pearson, N.J., 2012. Multi-stage origin of Roberts Victor eclogites: progressive metasomatism and its isotopic effects. Lithos 142, 161–181.

Imayama, T., Oh, C.-W., Baltybaev, S.K., Park, C.-S., Yi, K., Jung, H., 2017. Paleoproterozoic high-pressure metamorphic history of the Salma eclogite on the Kola Peninsula, Russia. Lithosphere 855–873, 2017.

Irvine, T.N., Baragar, W.R.A., 1971. A guide to the chemical classification of the common volcanic rocks. Can. J. Earth Sci. 8, 523–548.

Jackson, S.E., Pearson, N.J., Griffin, W.L., Belousova, E.A., 2004. The application of laser ablation-inductively coupled plasma-mass spectrometry to in situ U-Pb zircon geochronology. Chem. Geol. 211, 47–69.

Jacob, D.E., 2004. Nature and origin of eclogite xenoliths from kimberlites. Lithos 77, 295–316.

Jardim de Sá, E.F., 1994. A Faixa Seridó (Província Borborema, Ne Brasil) e o seu Significado Geodinâmico na Cadeia Brasiliana/Pan-Africana. Tese de Doutorado, Universidade De Brasília, 803 pp (in Portuguese).

Jochum, K.P., Seufert, H.M., Spettel, B., Palme, H., 1986. The solar system abundances of Nb, Ta and Y and the relative abundances of refractory lithophile elements in differentiated planetary bodies. Geochem. Cosmochim. Acta 50, 1173–1184.

Kiseeva, E.S., Kamenetsky, V.S., Yaxley, G.M., Shee, S.R., 2016. Mantle melting versus mantle metasomatism – "the chicken or the egg" dilemma. Chem. Geol. 455, 220-130.

Kohn, M., Corrie, S., Markley, C., 2015. The fall and rise of metamorphic zircon. Am. Mineral. 100, 897–908.

Korhonen, F., Brown, M., Clark, C., Bhattacharya, S., 2013. Osumilite–melt interactions in ultrahigh temperature granulites: Phase equilibria modelling and implications for the P-T–t evolution of the Eastern Ghats Province, India. Journal of Metamorphic Geology 31, 881–907.

Lanari, P., Engi, M., 2017. Local bulk composition effects on mineral assemblages. In: Kohn, M.J., Lanari, P., Engi, M. (Eds.), Petrochronology. Reviews in Mineralogy and Geochemistry, vol. 83, pp. 55–102.

Lanari, P., Riel, N., Guillot, S., Vidal, O., Schwartz, S., Pêcher, A., Hattori, K.H., 2013. Deciphering high-pressure metamorphism in collisional context using microprobe mapping methods: application to the Stak eclogitic massif (northwest Himalaya). Geology 41, 111–114.

Lanari, P., Giuntoli, F., Loury, C., Burn, M., Engi, M., 2017. An inverse modeling approach to obtain P-T conditions of metamorphic stages involving garnet growth and resorption. Eur. J. Mineral 29, 181–199.

Li, X., Zhang, L., Wei, C., Slabunov, A.I., 2015. Metamorphic PT path and zircon U–Pb dating of Archean eclogite association in Gridino complex, Belomorian province, Russia. Precambrian Res. 268, 74–96.

Liu, F., Zhang, L., Li, X., Slabunov, A.I., Wei, C., Bader, T., 2017. The metamorphic evolution of Paleoproterozoic eclogites in Kuru-Vaara, northern Belomorian Province, Russia: constraints from P-T pseudosections and zircon dating. Precambrian Res. 298, 31–47.

Loose, D., Schenk, V., 2018. 2.09 Ga old eclogites in the Eburnian-Transamazonian orogen of southern Cameroon: significance for Palaeoproterozoic plate tectonics. Precambrian Res. 304, 1–11.

Ludwig, K.R., 2008. User's manual for Isoplot 3.0. A geochronological toolkit for microsoft Excel. Berkeley Geochronol. Center 4 (4), 76.

McClelland, W.C., Lapen, T.J., 2013. Linking time to the pressure–temperature path for ultrahigh-pressure rocks. Elements 9, 273–279.

Meschede, M., 1986. A method of discrimination between different types of mid-ocean ridge basalts and continental tholeiites with the Nb-Zr-Y diagram. Chem. Geol. 56, 207–218.

Mints, M.V., Konilov, A.N., Dokukina, K.A., Kaulina, T.V., Belousova, E.A., Natapov, L.M., Griffin, W.L., O'Reilly, S.Y., 2010. The Belomorian eclogite province: unique evidence of Meso-Neoarchaean subduction and collision. Dokl. Earth Sci. 434, 1311–1316.

Morel, M.L.A., Nebel, O., Nebel-Jacobsen, Y.L., Miller, J.S., Vroon, P.Z., 2008. Hafnium isotope characterization of the GJ-1 zircon reference material by solution and laser-ablation MC-ICPMS. Chem. Geol. 255, 231–235.

Moyen, J.F., Martin, H., 2012. Forty years of TTG research. Lithos 148, 312–336.

Nebel, O., Nebel-Jacobsen, Y., Mezger, K., Berndt, J., 2007. Initial Hf isotope compositions in magmatic zircon from early Proterozoic rocks from the Gawler Craton, Australia: a test for zircon model ages. Chem. Geol. 241, 23–37.

Oliveira, R.G., Medeiros, W.E., 2018. Deep crustal framework of the Borborema Province, NE Brazil, derived from gravity and magnetic data. Precambrian Res. 315, 45–65.

Padilha, A.L., Vitorello, Í., Pádua, M.B., Fuck, R.A., 2017. Cryptic signatures of Neoproterozoic accretionary events in northeast Brazil imaged by magnetotellurics: implications for the assembly of West Gondwana. Tectonophysics 699, 164–177.

Palin, R.M., White, R.W., 2016. Emergence of blueschist on Earth linked to secular changes in oceanic crust composition. Nat. Geosci. 9, 60–64.

Patchett, J.P., 1983. The importance of the Lu–Hf isotopic system in studies of planetary chronology and chemical evolution. Geochem. Cosmochim. Acta 47, 81–91.

Pearce, J.A., 1996. A User's Guide to Basalt Discrimination Diagrams. In: Wyman, D.A., Ed., Trace Element Geochemistry of Volcanic Rocks: Applications for Massive Sulphide Exploration, Geological Association of Canada, Short Course Notes, 12, 79–113.

Pearce, J.A., 2008. Geochemical fingerprinting of oceanic basalts with applications to ophiolite classification and the search for Archean oceanic crust. Lithos 100, 14–48.

Pearce, J.A., Gorman, B.E., Birkett, T.C., 1975. The TiO_2 - K_2O - P_2O_5 diagram: a method of discriminating between oceanic and non- oceanic basalts. Earth Planet Sci. Lett. 24, 419–426.

Plank, T., 2005. Constraints from thorium/lanthanum on sediment recycling at subduction zones and the evolution of the continents. J. Petrol. 46, 921–944.

Polat, A., 2012. Growth of Archean continental crust in oceanic island arcs. Geology 40, 383–384.

Polat, A., Fryer, B., Samson, I.M., Weisener, C., Appel, P.W.U., Frei, R., Windley, B.F., 2011. Geochemistry of ultramafic rocks and hornblendite veins in the Fiskenæsset layered anorthosite complex, SW Greenland: evidence for hydrous upper mantle in the Archean. Precambrian Res. 214–215, 124–153.

Powell, R., Holland, T.J.B., 2008. On thermobarometry. J. Metamorph. Geol. 26, 155–179.

Reno, B.L., Piccoli, P.M., Brown, M., Trouw, R.A.J., 2012. In situ monazite (U-Th)-Pb ages from the Southern Brasília Belt, Brazil: constraints on the high-temperature retrograde evolution of HP granulites. J. Metamorph. Geol. 30, 81–112.

Rollinson, H., 2010. Coupled evolution of Archean continental crust and subcontinental lithospheric mantle. Geology 38, 1083–1086.

Rubatto, D., Gebauer, D., 2000. Use of cathodoluminescence for U–Pb zircon dating by ion microprobe: some examples from the Western Alps. In: Pagel, M., Barbin, V., Blanc, P., Ohnenstetter, D. (Eds.), Cathodoluminescence in Geosciences. Springer, Berlin, Heidelberg, pp. 373–400. https://doi.org/10.1007/978-3-662-04086-7_15.

Rubatto, D., Hermann, J., 2001. Exhumation as fast as subduction? Geology 29 (1), 3–6.

Rubatto, D., Hermann, J., Buick, I.S., 2006. Temperature and bulk composition control on the growth of monazite and zircon during low-pressure anatexis (Mount Stafford, central Australia). J. Petrol. 47, 1973–1996.

Rudnick, R.L., Gao, S., 2003. The composition of the continental crust. In: Rudnick, R.L., Holland, H.D., Turekian, K.K. (Eds.), Treatise on Geochemistry - the Crust. Elsevier, Oxford, pp. 1–64.

Santos, T.J.S., Fetter, A.H., Nogueira Neto, J.A., 2008. Comparisons between the northwestern Borborema province, NE Brazil, and the southwestern Pharusian Dahomey belt, SW central Africa. In: Pankhurst, R.J., Trouw, R.A.J., Brito Neves, B.B., de Wit, M.J. (Eds.), West Gondwana: Pre-Cenozoic Correlation across the South Atlantic Region. Geol. Soc. Lond. Spec. Publ, 294, 101–120.

Santos, T.J.S., Garcia, M.G.M., Amaral, W.S., Caby, R., Wernick, E., Arthaud, M.H., Dantas, E.L., Santosh, M., 2009. Relics of eclogite facies assemblages in the Ceará central domain, NW Borborema province, NE Brazil: implications for the assembly of West Gondwana. Gondwana Res. 15, 454–470.

Santos, T.J.S., Amaral, W.S., Ancelmi, M.F., Pitarello, M.Z., Fuck, R.A., Dantas, E.L., 2015. U–Pb age of the coesite-bearing eclogite from NW Borborema Province, NE Brazil: implications for western Gondwana assembly. Gondwana Res. 28, 1183–1196.

Scherer, E., Münker, C., Mezger, K., 2001. Calibration of the lutetium-hafnium clock. Science 293, 683–687.

Shervais, J.W., 1982. Ti-V plot and the petrogenesis of modern and ophilitic lavas. Earth Planet Sci. Lett. 59, 101–118.

Sizova, E., Gerya, T., Brown, M., 2014. Contrasting styles of Phanerozoic and Precambrian continental collision. Gondwana Res. 25, 522–545.

Souza, Z.S., Martin, H., Peucat, J.J., Jardim de Sá, E.F., Macedo, M.H.F., 2007. Calc-alkaline magmatism at the archean-proterozoic transition: the Caicó complex basement (Ne Brasil). J. Petrol. 48, 2149–2185.

Sun, S.S., McDonough, W.F., 1989. Chemical and Isotopic Systematics of Oceanic Basalts: Implications for Mantle Composition and Processes. Geol. Soc. Lond. Spec. Publ, 42, 313–345.

Tedeschi, M., Lanari, P., Rubatto, D., Pedrosa-Soares, A., Hermann, J., Dussin, I., Pinheiro, M.A.P., Bouvier, A.S., Baumgartner, L., 2017. Reconstruction of multiple P-T-t stages from retrogressed mafic rocks: subduction versus collision in the Southern Brasília orogen (SE Brazil). Lithos 294–295, 283–303.

Tichomirowa, M., Whitehouse, M.J., Nasdala, L., 2005. Resorption, growth, solid state recrystallisation, and annealing of granulite facies zircon—a case study from the Central Erzgebirge, Bohemian Massif. Lithos 82, 25–50.

Trindade, R.I.F., Dantas, E.L., Babinski, M., Van Schmus, W.R., 1999. Short-lived granitic magmatism along shear zones: evidence from U-Pb zircon and sphene ages of Caraúbas and Tourão granites. In: Actas. Cordoba: SEGEMAR.

Trouw, R.A.J., Peternel, R., Ribeiro, A., Heilbron, M., Vinagre, R., Duffles, P., Trouw, C.C., Fontainha, M., Kussama, H.H., 2013. A new interpretation for the interference zone between the southern Brasília belt and the central Ribeira belt, SE Brazil. J. S. Am. Earth Sci. 48, 43–57.

Van Schmus, W.R., Oliveira, E.P., Silva Filho, A.F., Toteu, S.F., Penaye, J., Guimarães, I.P., 2008. Proterozoic links between the Borborema Province, NE Brazil, and the Central African Fold Belt. Geol. Soc. Lond. Spec. Publ, 294, 69–99.

Vervoort, J.D., Blichert-Toft, J., 1999. Evolution of the depleted mantle: Hf isotope evidence from juvenile rocks through time. Geochem. Cosmochim. Acta 63, 533–556.

Wang, H., Liu, F., Li, J., Sun, Z., Ji, Tian, Z., Liu, L., Santosh, M., 2019. Petrology, geochemistry and P–T–t path of lawsonite-bearing retrograded eclogites in the Changning–Menglian orogenic belt, southeast Tibetan Plateau. J. Metamorph. Geol. 37, 439–478.

Waters, D., 2003. P-T path from Cpx-Hbl-Pl symplectites. www.earth.ox.ac.uk/~dawewa/index.html.

Wedepohl, K.H., 1995. The compositions of the continental crust. Geochem. Cosmochim. Acta 59, 1217–1232.

Weller, O.M., St-Onge, M.R., 2017. Record of modern-style plate tectonics in the Palaeoproterozoic Trans-Hudson orogeny. Nat. Geosci. 10, 305–311.

White, R.W., Powell, R., Baldwin, J.A., 2008. Calculated phase equilibria involving chemical potentials to investigate the textural evolution of metamorphic rocks. J. Metamorph. Geol. 26, 181–198.

Whitney, D.L., Evans, B.W., 2010. Abbreviations for names of rock-forming minerals. Am. Mineral. 95, 185–187.

Willbold, M., Stracke, A., 2010. Formation of enriched mantle components by recycling of upper and lower continental crust. Chem. Geol. 276, 188–197.

Wood, D.A., 1980. The Application of Th-Hf-Ta diagram in problems of tectonomagmatic classification and to establishing the nature of crustal contamination of basaltic lavas of the British Tertiary volcanic province. Earth Planet Sci. Lett. 50, 11–30.

Yakymchuk, C., Brown, M., 2019. Divergent behaviour of Th and U during anatexis: implications for the thermal evolution of orogenic crust. J. Metamorph. Geol. 2019 (37), 899–916.

Zeh, A., Gerdes, A., Klemd, R., Barton Jr., J.M., 2007. Archaean to Proterozoic crustal evolution in the central zone of the Limpopo Belt (South Africa-Botswana): constraints from combined U-Pb and Lu-Hf isotope analyses of zircon. J. Petrol. 48, 605-1639.

Zhang, C., Zhang, L., Bader, T., Song, S., Lou, Y., 2013. Geochemistry and trace element behaviors of eclogite during its exhumation in the Xitieshan terrane, North Qaidam UHP belt, NW China. J. Asian Earth Sci. 63, 81–97.

Zhang, L., Zhang, Z., Schertl, H.P., Wei, C., 2019. HP–UHP metamorphism and tectonic evolution of orogenic belts: introduction. Geol. Soc. Lond. Spec. Publ. 474, 1–4.